Hybrid Electric Vehicle Fuel Minimization by DC-DC Converter Dual-Phase-Shift Control

Simos A. Evangelou[a], M. A. Rehman-Shaikh[b]

[a] Department of Electrical and Electronic Engineering, Imperial College London, UK
[b] Hamilton Machine Tools, Cheshire, UK

Abstract

The paper introduces an advanced DC-link variable voltage control methodology that improves significantly the fuel economy of series Hybrid Electric Vehicles (HEVs). The DC-link connects a rectifier, a Dual Active Bridge (DAB) DC-DC converter and an inverter, interfacing respectively the two sources and the load in a series HEV powertrain. The introduced Dual Phase Shift (DPS) proportional voltage conversion ratio control scheme is realized by manipulating the phase shifts of the gating signals in the DAB converter, to regulate the amount of DAB converter power flow in and out of the DC-link. Dynamic converter efficiency models are utilized to account for switching, conduction, copper and core losses. The control methodology is proposed on the basis of improving the individual efficiency of the DAB converter but with its parameters tuned to minimize the powertrain fuel consumption. Since DPS control has one additional degree of freedom as compared to Single Phase Shift (SPS) voltage control schemes, a Lagrange Multiplier optimization method is applied to minimize the leakage inductance peak current, the main cause for switching and conduction losses. The DPS control scheme is tested in simulations with a full HEV model and two associated conventional supervisory control algorithms, together with a tuned SPS proportional voltage conversion ratio control scheme, against a conventional PI control in which the DC-link voltage follows a constant reference. Nonlinear coupling difficulties associated with the integration of varying DC-link voltage in the powertrain are also exposed and addressed.

Keywords:
Hybrid electric vehicles, fuel minimization, DC-DC converter control, dual-phase-shift control

Abbreviations

DAB	Dual Active Bridge
DPS	Dual Phase Shift
HEV	Hybrid Electric Vehicle
ICE	Internal Combustion Engine
PFC	Power Follower Control
PL	Propulsion Load
PMSG	Permanent Magnet Synchronous Generator
PMSM	Permanent Magnet Synchronous Motor
PS	Primary Source of energy
SCS	Supervisory Control System
SOC	State Of Charge
SPS	Single Phase Shift
SS	Secondary Source of energy
TCS	Thermostat Control Strategy

1. Introduction

Transport is a significant contributor of carbon emissions, only coming second to Energy [1]. The vast majority of these emissions come from road transport and are currently on the rise [2]. The hybrid electric vehicle (HEV) has been identified as critical for achieving sustainable transportation, by decreasing consumption of fossil fuels [3]. According to [4] there is a strong potential to enhance the sustainable impact of HEVs by improving their efficiency, with significant advances already achieved in the last decade by smart supervisory control systems that manage the powertrain energy flow[5]. The present paper represents an attempt to contribute to this goal by proposing DC-link voltage controls to operate series HEV powertrains more efficiently and improve their fuel economy.

Various HEV topologies exist. A DC-DC converter is included in architectures in which the DC-link and electric energy store (generally a chemical battery) operate at different voltages, to act as the interface between them. Many types of DC-DC converters have already been employed in this context, ranging from standard boost [6], three-level [7], isolated dual half- and full-bridge (DAB) [8–12] and other converters [13]. The DAB converter, included in the present research, has become popular due to its advantages in power controllability, bi-directionality, soft-switching ability and high efficiency [14]. Operation under soft-switching has particularly received wide attention in an attempt to achieve energy loss minimization [15, 16]. The loss reduction is achieved by zero-voltage-switching (ZVS) or zero-current-switching (ZCS) in all the converter switches, but this comes at the expense of additional components and more complex control. Furthermore, the reduction is obtained mainly in the switching losses which is only one of the loss mechanisms in the converter.

The simplicity and ease of implementation of the single phase-shift (SPS) control has established it as the classical con-

Email addresses: s.evangelou@imperial.ac.uk (Simos A. Evangelou), hamiltontools@aol.com (M. A. Rehman-Shaikh)

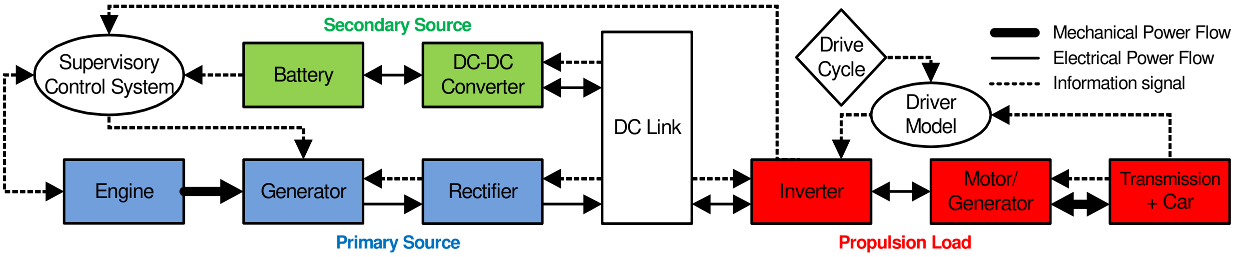

Figure 1: High level block diagram of the series HEV powertrain used in this work [17].

trol methodology of DAB converters. In this scheme, the average power flow through the converter can be regulated directly by the phase shift input. However, operation under SPS control is marred by circulating currents and reactive power, which increase the energy losses [18]. Various other control algorithms, involving different phase-shift and modulation strategies, have been proposed in the literature with the aim of increasing the DAB converter efficiency [19–21]. These schemes, however, have disadvantages related to implementation complexity, limited power range and limited operating range. Dual phase-shift (DPS) control, which manipulates two phase-shifts as control inputs, has emerged as a suitable algorithm to eliminate reactive power and increase efficiency [18, 22, 23].

Beyond the provision of the interface, the deployment of a DC-DC converter in a series HEV powertrain facilitates the controlled variation of the DC-link voltage by manipulating the converter electronic switches via their gating signals. Studies on DC-link control already exist, with a precursor of such work found in [6]. This work compares two single source electric drive systems in which a battery either supplies an inverter directly or does so via a bidirectional boost converter, to power a Permanent Magnet Synchronous Motor (PMSM). The presence of the boost converter enables control of the DC-link voltage, and it is shown that when the voltage is changed in proportion with the PMSM speed, overall efficiency improvements result.

In [24] a more complex dual source topology is considered corresponding to series HEV powertrains. It comprises a DC-link with a three-phase rectifier interfaced engine-generator set, a bidirectional DC-DC converter interfaced battery, and a three-phase inverter interfaced motor. The work proposes improved operation reliability by implementing DC-link voltage control which maintains a constant inverter modulation index. The principle followed is that reliability deteriorates with increasing converter energy losses, hence the underlining objective of the DC-link control is to reduce these losses. However, while the constant modulation index objective is beneficial to the inverter losses, it is not necessarily the optimal rule for DC-DC converter loss reduction. Furthermore, [24] does not account for the rectifier losses and the effect of the voltage control on these losses.

A similar series HEV powertrain, with a DAB DC-DC converter, is treated in [25] with the objective to reduce the losses in all the electronic converters. This work develops a process to choose the most appropriate nominal DC-link voltage for maximized inverter and rectifier efficiencies. It also designs a DC-link voltage control that pushes the DAB converter in boost/buck operation when the battery charges/discharges, such that it avoids hard switching losses persistently in its whole operating range. Thus it achieves substantially higher converter efficiency than conventional constant voltage control schemes. Nevertheless, this study does not consider the impact of the varying DC-link voltage on the overall efficiency of the powertrain and hence on the fuel economy.

The present research develops a novel, efficient and powerful DC-link voltage control algorithm for a series HEV that optimizes the overall system efficiency, by dual-phase-shift control of the DAB DC-DC converter. In order to provide the appropriate context for comparison the research also contributes a single-phase-shift algorithm for DC-link control, based on the approach in [25], which has further been adapted and optimized for overall system efficiency. System efficiency is quantified by utilizing the concept of equivalent fuel consumption which accounts for both the real fuel and battery charge consumption. Both control schemes developed are compared with a conventional PI constant DC-link voltage control scheme in extensive simulations with a comprehensive HEV mathematical model. The investigation in this paper represents an application of DPS control in a significantly more complex setting than in existing literature, which essentially considered DPS control of a DAB DC-DC converter utilized at simple boundary conditions of constant input voltage and constant power out to a resistive load [22, 23, 26, 27].

The paper structure is as follows. Section 2 describes: (a) the basis HEV model that is used to conduct the research, (b) the supervisory control strategies employed to simulate the HEV model, (c) the modeling of the inverter and rectifier power loss respectively for varying PMSM and Permanent Magnet Synchronous Generator (PMSG) operating conditions, and (d) the operating mode dependent DAB converter switching, conduction, copper and core loss modeling. Section 3 describes the DC-link control schemes developed and tested in this work: the constant voltage PI control, and the SPS and DPS proportional voltage conversion ratio control schemes. Simulation results are presented in Section 4, including a description of the tuning of the voltage controls, and a comparison of their characteristics and performance in terms of power profile, evolution of DC-link voltage and modulation indexes, converter losses and fuel economy. Conclusions are drawn in Section 5.

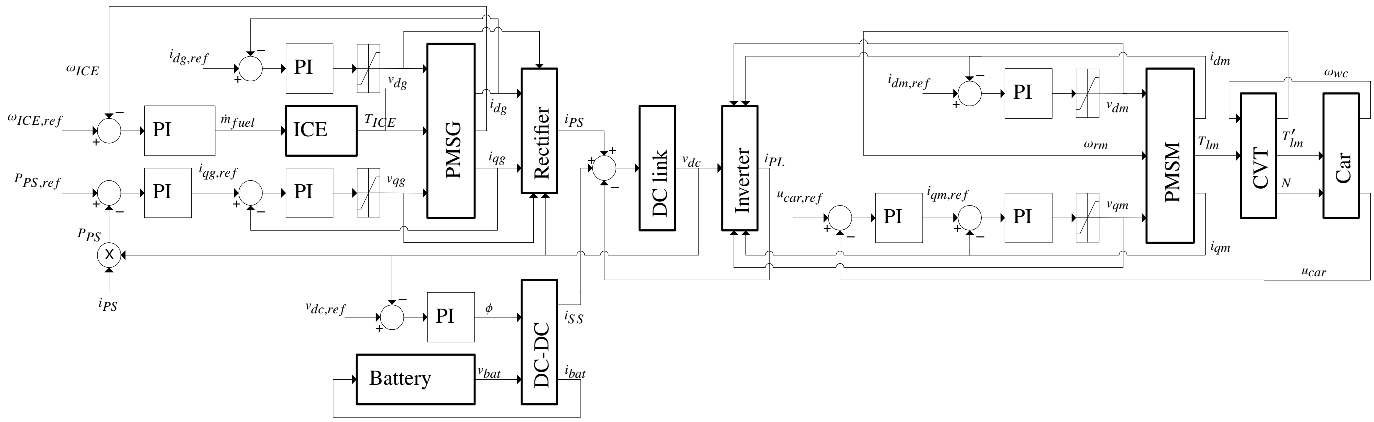

Figure 2: Specific block diagram showing the interconnection of the internal combustion engine (ICE), PMSG, rectifier, battery, DC-DC converter, inverter, PMSM, continuously variable transmission (CVT) and car, and the related control loops [17].

2. Modeling

The HEV model utilized in this paper is high-fidelity. It corresponds to a general-purpose passenger car and is based on that presented in [25] and [28], with earlier versions of the model found in [17] and [29]. As in the basis model, the present model characterizes the dynamic efficiency for both the inverter and rectifier by including modulation-index dependent conduction and switching losses. The DAB converter design employed in this work reduces the emphasis on soft switching and hence a corresponding concise loss model is utilized, which has been developed in [30] and is based on the model in [22]. The HEV model, supervisory control schemes, and inverter, rectifier and DC-DC converter dynamic efficiency models employed are summarised in this section.

2.1. Vehicle Model

The overall structure of the HEV powertrain is shown in Fig. 1, and a block diagram with the physical interconnections of the components and control loops, is shown in Fig. 2.

The powertrain includes a primary (PS) and a secondary (SS) energy source, which individually or jointly satisfy the demanded propulsion load (PL) via a common DC-link. A circuit diagram of the electrical interconnections of the components at the DC-link is shown in Fig. 3. The PS is a turbocharged 2.0L diesel engine driving a PMSG and supplying power to a three-phase rectifier. The SS is a lithium-ion battery powering a bi-directional DC-DC converter. The PL is a three-phase inverter driven PMSM relaying torque to the wheels via a continuously variable transmission. As described in [17], the direct current of both the PMSM and PMSG is controlled to 0 A, by setting the $i_{dm,ref}$ and $i_{dg,ref}$ reference currents (shown in Fig. 2) to 0 A. The respective PMSM and PMSG quadrature currents are controlled to vary the torque such that the required vehicle speed and PMSG power output are achieved. Regenerative braking is also available; kinetic energy from the wheels is converted into electrical energy by the PMSM which acts as a PMSG, and is stored in the battery.

In previous work, a constant DC-link voltage has been maintained by a PI control loop [17, 28], as shown in Fig. 2, or it has been varied according to the more advanced and efficient SPS proportional voltage conversion ratio control scheme for the DC-DC converter [25]. The proportion of power served to the load by the PS is determined by the reference power $P_{PS,ref}$ (see Figs. 2 and 3), while any remaining or excess power proportion is respectively supplied or absorbed by the battery. Thus, $P_{PS} + P_{SS} = P_{PL}$, where P_{PS} and P_{SS} are respectively the output powers of the PS and SS, and P_{PL} is the load power demanded by the PL.

The $P_{PS,ref}$ value is decided by an outer supervisory control system (SCS), according to the SOC of the battery and the motor load. In any case, the PS and SS are operated within operational and physical constraints of $P_{PS} < 58$ kW and -21 kW$< P_{SS} < 42$ kW, where negative SS power corresponds to charging either from the ICE or regenerative braking. To protect the battery, the SOC is operated by the SCS between the constraints $SOC_L = 50\%$ and $SOC_U = 80\%$, and is initialized at 65% (mid-point between the limits).

A start-stop system (SSS) is also included in the vehicle which enables switching off the ICE to reduce idling losses, where a fuel mass penalty of 0.00011 kg per engine switching event has been used. Furthermore, any given SCS is not required to control the ICE speed because that is optimally controlled for each PS power by a separate engine controller, which is typical for series HEVs in which the ICE is not mechanically connected to the wheels.

2.2. Supervisory Control Strategies

Two popular SCSs are utilized to simulate the HEV model, the Thermostat and the Power Follower control strategies, to give a broad perspective of the capability of the voltage control schemes studied in this paper.

The Thermostat (TCS) SCS is the most conventional series HEV control strategy [31, 32]. It is robust, simple and leads to good fuel economy. It works according to the principle of operating the PS either at its most efficient point with the SS acting as an equalizer, or idling at zero power with all the demanded power provided by the SS. The former mode of operation is active until the SOC upper threshold of 80% is reached, at which

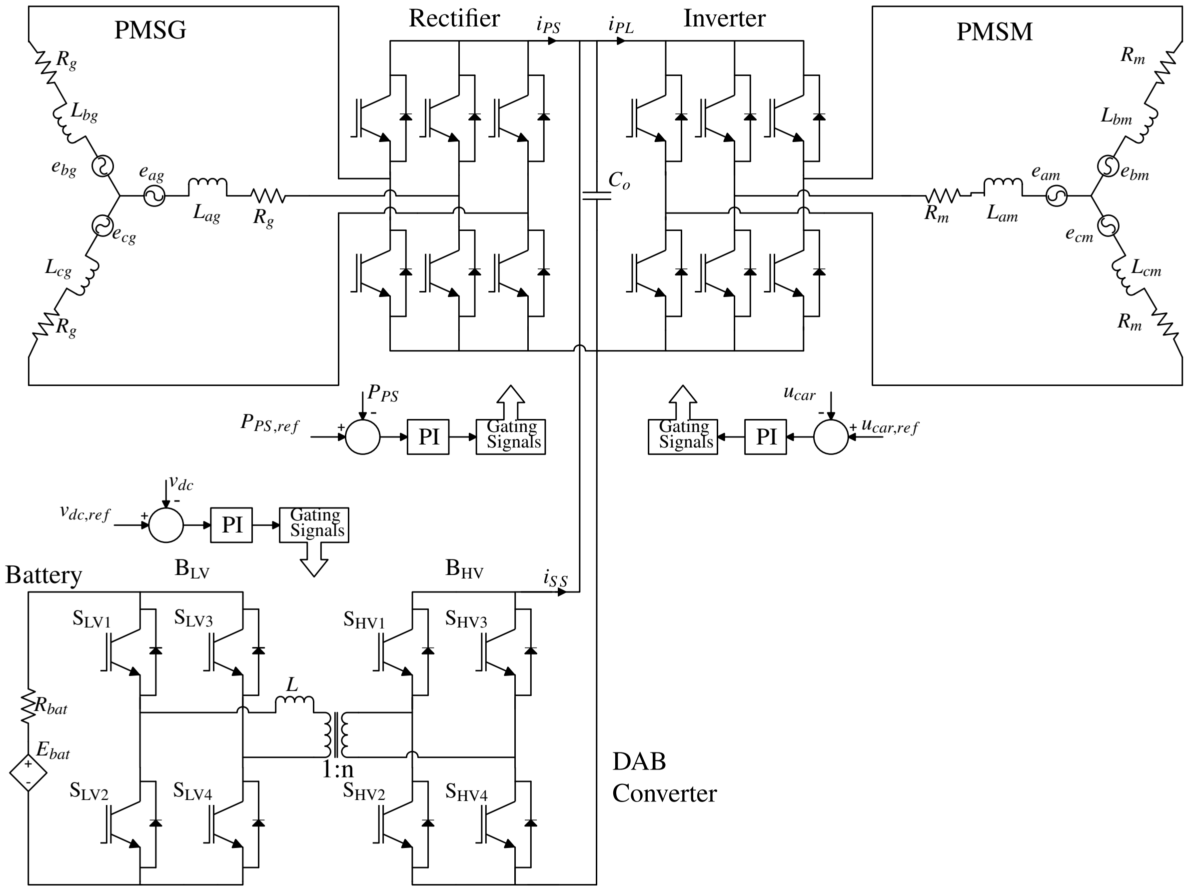

Figure 3: The series HEV powertrain includes the PMSG, rectifier, battery, DAB converter, inverter and PMSM, as illustrated by the circuit diagram. Symbols R, L and e represent phase resistances, inductances and induced emfs respectively. Subscripts a, b and c correspond to the individual phases, and subscripts g, m and ref correspond to 'generator', 'motor' and 'reference'. E_{bat} and R_{bat} correspond to the battery emf and internal resistance, while L is the inductance associated with the DC-DC converter and C_0 is the DC-link capacitance. i_{PS}, i_{SS} and i_{PL} are the primary source (PMSG-branch), secondary source (battery-branch) and propulsion load (PMSM-branch) DC currents. The control signals are v_{dc} (the DC-link voltage), P_{PS} (the primary source power) and u_{car} (the forward speed of the car).

time the SS-only operating mode is entered. After this the SOC is depleted quickly and once it falls to the lower threshold of 50% the SCS re-enters the optimal PS operation mode. The optimal $P_{PS\,opt}$ was found in earlier work to be 19.8 kW [28, 33]. When the PL demand exceeds this power, both the PS and SS supply power at the same time in hybrid mode. Moreover, when there is large regenerative braking power (negative P_{PL}) the PS reduces its supplied power to a lower level (tuned in previous work at $P_{PS\,min} = 7$ kW [28]).

The Power Follower (PFC) is the second most conventional SCS applied to series HEVs. In this strategy, PS power generally follows the demand of the PL, when the SOC is at the nominal value of 65%, but it deviates, in hybrid operation with the battery, towards charging or discharging the battery when SOC is low and high respectively. In the latter case P_{PS} is given by $P_m(t) = P_{PL} + P_{ch}\,(SOC_{initial} - SOC(t))$, where P_{ch} is a parameter that can be tuned. Alternatively, the SS delivers power to the vehicle alone when the inverter demand (P_{PL}) is low and SOC high, and conversely the PS is selected to deliver power when P_{PL} is high or SOC is low. In any case when it is on, the PS operates within constraints given by $P_{min} \leq P_{PS} \leq P_{PS\,max}$, in which P_{min} is a parameter that can be tuned and $P_{PS\,max}$ corresponds to a physical PS constraint mentioned earlier. For the vehicle employed in the present work $P_{ch} = 0$ and $P_{min} = 16.8$ kW are used, which were found to be optimal for the basis model [28].

2.3. Inverter and Rectifier

The inverter and rectifier are assumed to operate by a standard three-phase sinusoidal Pulse Width Modulation (PWM) [34]. Their design is essentially the same, as shown in Fig. 3, but their functionality is generally opposite. In the present scheme, the inverter is bi-directional and normally converts DC to three-phase AC to power the PMSM, but it can also operate in reverse during regenerative braking. The rectifier converts power only in one direction, from three-phase AC to DC. An average model for each of these converters is employed, as has been described in [17]. Operation under linear modulation is desirable, in which the amplitude of the modulating signals does not exceed the amplitude of the high-frequency triangular carrier signal. Hence the modulation index, given by $M = 2\sqrt{v_{d*}^2 + v_{q*}^2}/v_{dc}$, is constrained to $0 \leq M \leq 1$, where the square root term is the amplitude of AC phase voltage, v_{dc} is the DC-link voltage, and the $*$ can be substituted by either 'm'

or 'g' for motor or generator respectively to correspond to direct and quadrature voltages (see Fig. 2). In the model this is achieved by using saturation functions to constrain v_{d*} and v_{q*}. These constraints vary as the DC-link voltage varies.

The efficiency of the inverter is introduced through the description of its total losses comprising conduction and switching losses. The inverter conductions losses are calculated by [25, 35, 36]:

$$P_{cond} = 6\Bigg(i_{pk}v_{f0}\left(\frac{1}{2\pi} - \frac{M}{8}\right) + i_{pk}^2 r_f\left(\frac{1}{8} - \frac{M}{3\pi}\right) + r_{ce}i_{pk}^2\left(\frac{1}{8} + \frac{M}{3\pi}\right) + v_{c0}i_{pk}\left(\frac{1}{2\pi} + \frac{M}{8}\right)\Bigg), \quad (1)$$

where $i_{pk} = \sqrt{i_{d*}^2 + i_{q*}^2}$ is the peak AC current from the inverter (where $*$ has the same meaning as previously to correspond to direct or quadrature currents, applicable also in the case of the rectifier), v_{f0} is the forward voltage of the diode at zero current, r_f is the forward resistance of the diode, r_{ce} is the collector emitter resistance of the IGBT and v_{c0} is the forward voltage of the IGBT at zero collector current. The inverter switching losses are determined by [25, 36]:

$$P_{sw} = 6\frac{f_i v_{dc} i_{pk}}{v_{ref} i_{ref} \pi}\left(E_{on,ref} + E_{off,ref} + E_{rr,ref}\right), \quad (2)$$

with f_i the inverter switching frequency, $E_{on,ref}$ the reference turn on energy loss of the IGBT, v_{ref} the voltage at which the reference energy loss is measured, i_{ref} the current at which the reference energy loss is measured, $E_{off,ref}$ the reference turn off energy loss of the IGBT and $E_{rr,ref}$ the reference reverse recovery energy loss of the diode. Reference and other parameter values of the IGBT and diode are obtained from the relevant datasheet. The conduction and switching losses of the rectifier are computed by the same expressions as for the inverter, but employing rectifier variables.

The switching frequencies of the inverter and rectifier are 20 kHz. The IGBT modules for both converters are selected from the Infineon range, by consideration of the voltage switched, and the peak and RMS current though each switch [37]. The worst case currents are computed according to the powertrain and vehicle operating envelope encapsulated by the driving cycles introduced in Section 4. Module FS150R12KT4 (with maximum blocking voltage of 1200 V, and continuous and peak currents of 150 A and 300 A respectively) is selected for all the switches in the two converters, with its relevant parameters extracted from the datasheet.

2.4. DC-DC Converter

A suitable DC-DC converter for the required power range transported in and out of the SS is the isolated bidirectional DC-DC converter, employing a DAB topology, as shown in Fig. 3. It consists of a low- (B_{LV}) and a high- (B_{HV}) voltage full bridges connected by an isolation transformer, comprising respectively S_{LV1}-S_{LV4} and S_{HV1}-S_{HV4} electronic switches. The inductor L corresponds to the sum of the auxiliary and transformer leakage inductances referred to the low-voltage (LV) side. The voltage conversion ratio, d, of the DAB converter is an important variable and is given by

$$d = \frac{v_{dc}}{n v_{bat}}, \quad (3)$$

where v_{bat} (battery voltage) is the input voltage of the converter, v_{dc} (DC-link voltage) is the output voltage of the converter and n is the turns ratio of the transformer. When d is greater/less that 1 the DAB converter is operating in boost/buck mode [38].

A common control scheme adopted for the DAB converter is the single phase-shift control. In this scheme the phase shift ϕ between gating signals in the two bridges, of constant 0.5 duty cycle, regulates directly the average transmission power of the converter, both in direction and magnitude. Power flows from the LV (battery) side to the high-voltage (HV) (DC-link) side for positive phase shift, and vice versa for negative phase shift to charge the battery, for example.

Another DAB converter control approach is by dual phase-shift control, which underpins the scheme developed in the present work. This method commands two phase shifts in the converter, the D_1 (inner) and D_2 (outer) phase shifts. D_2 is the gating signal phase shift for any two devices across the two bridges, for example S_{LV1} and S_{HV1}, and is identical in meaning to the single phase-shift ϕ. D_1 corresponds to the gate control signal phase shift of same-bridge opposite-corner switching devices, such as S_{LV1} and S_{LV4}. All the switches in a DPS scheme are operated with the same duty cycle of 0.5 as in SPS implementations. The utilization of two phase shifts in DPS generates additional operating modes in comparison to SPS. On the whole, the D_1 and D_2 phase-shift pair alone determines the DPS modes, as shown in Table 1 and Fig. 4. Note that, the forward ($D_2 \geq 0$) or reverse ($D_2 < 0$) power flow cases are considered in the literature essentially only individually, but here the whole operating range is treated at once as there is significant power flow in both directions.

Table 1: DPS operating modes with respect to D_1 and D_2.

Mode	Boundary 1	Boundary 2	Boundary 3
$M1_P$	$D_2 \geq 0$	$D_1 < D_2$	$D_1 + D_2 \geq 1$
$M2_P$	$D_2 \geq 0$	$D_1 < D_2$	$D_1 + D_2 < 1$
$M3_P$	$D_2 \geq 0$	$D_1 \geq D_2$	$D_1 + D_2 < 1$
$M4_P$	$D_2 \geq 0$	$D_1 \geq D_2$	$D_1 + D_2 \geq 1$
$M1_N$	$D_2 < 0$	$D_1 < \lvert D_2 \rvert$	$D_1 + \lvert D_2 \rvert \geq 1$
$M2_N$	$D_2 < 0$	$D_1 < \lvert D_2 \rvert$	$D_1 + \lvert D_2 \rvert < 1$
$M3_N$	$D_2 < 0$	$D_1 \geq \lvert D_2 \rvert$	$D_1 + \lvert D_2 \rvert < 1$
$M4_N$	$D_2 < 0$	$D_1 \geq \lvert D_2 \rvert$	$D_1 + \lvert D_2 \rvert \geq 1$

Table 2 provides the definitions of the various symbols and their values used in the DAB converter model. The analytical expressions of the average output power for all the converter modes are given in Table 3 [23]. A surface plot in Fig. 5 shows how the converter output power varies with D_1 and D_2 for three exemplary cases of voltage conversion ratio. It is clear from this plot that modes $M2_P$, $M2_N$, $M3_P$, and $M3_N$ offer access to the full power range. It is also known that these modes are the most suitable for optimal operation due to better characteristics

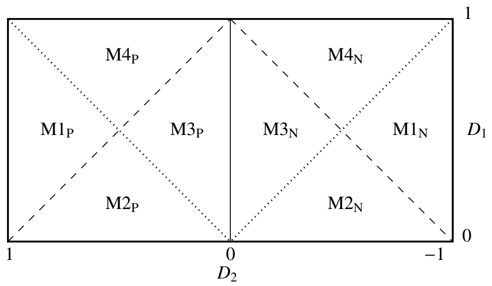

Figure 4: DPS operating modes with respect to D_1 and D_2. The boundaries $D_1 = |D_2|$ and $D_1 + |D_2| = 1$ are shown respectively by the dotted and dashed lines.

Table 2: DAB Converter Parameters (LV-side referred where relevant)

	Definition	Value (SI Units)
f_s	DAB Switching Frequency	20×10^3
L	Transf. Leakage + Auxiliary Inductance	10×10^{-6}
n	Transformer Turns Ratio	2.18
N_1	Number of Primary Transformer Turns	10
R	Transf. + Auxiliary Inductor Resistance	0.025
K	Transformer Core Loss Parameter	150
l_g	Transformer Air Gap Length	1.5×10^{-3}
V_c	Transformer Core Volume	3.72×10^{-5}
μ_0	Permeability of Free Space	$4\pi \times 10^{-7}$

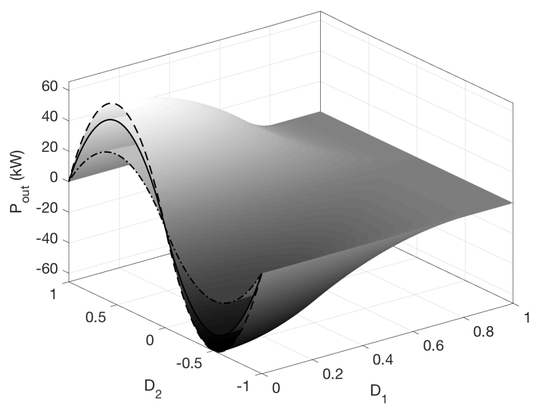

Figure 5: DAB converter output power variation with D_1 and D_2 for three d values: 0.6 (dash-dotted), 1 (solid), 1.2 (dashed).

Table 3: DAB converter average output power.

Converter Mode	P_{out}
M1_P and M1_N	$\frac{v_{bat}^2}{4f_sL}d(1-\lvert D_2\rvert)(1+\lvert D_2\rvert-2D_1)\,\text{sign}(D_2)$
M2_P and M2_N	$\frac{v_{bat}^2}{4f_sL}d(-D_1^2-2D_2^2+2\lvert D_2\rvert)\,\text{sign}(D_2)$
M3_P and M3_N	$\frac{v_{bat}^2}{4f_sL}d(2-2D_1-\lvert D_2\rvert)D_2$
M4_P and M4_N	$\frac{v_{bat}^2}{4f_sL}d(1-D_1)^2\,\text{sign}(D_2)$

in terms of peak and rms currents [23]. Therefore the present work will focus only on these modes. Analytical expressions for peak and rms currents are shown in Table 4 for M2_P, M2_N, M3_P and M3_N, with all quantities and parameters referred to the LV side. Average absolute currents (referred to LV side) are also derived for M2_P, M2_N, M3_P, and M3_N from the inductor current $i_\text{L}(t)$ according to,

$$i_{\text{ave}} = \frac{1}{T_{\text{sh}}}\int_0^{T_{\text{sh}}} |i_\text{L}(t)|\,dt, \tag{4}$$

in which $T_{\text{sh}} = 1/(2f_s)$ is the half switching period [22, 30].

2.4.1. Power loss model

DAB converter losses comprise IGBT/diode conduction and switching losses, and transformer/auxiliary-inductor copper and core losses.

The conduction losses are calculated from i_{ave} by adding the individual losses of all the devices in both bridges that are on within a half switching cycle, and further assuming equal forward voltage drops in IGBTs (V_{CEsat}) and diodes [22, 30]:

$$P_{\text{conduction}} = \frac{2(n+1)}{n}V_{\text{CEsat}}i_{\text{ave}}. \tag{5}$$

Switching losses consist of soft- and hard-switching losses. The present model recognizes that the former losses are a much smaller component and it therefore neglects the soft-switching losses. It also assumes that the hard-switched switches reduce their current linearly to zero during turn-off, and reduce their voltage linearly to zero during turn-on. Consequently, it estimates device switching loss from the switched voltage, the switching instant peak currents, and the switching event turn-off and turn-on times [22, 30].

The copper losses of the transformer and auxiliary inductor can be calculated from i_{rms} as follows:

$$P_{\text{copper}} = Ri_{\text{rms}}^2. \tag{6}$$

The core losses of the transformer and auxiliary inductor can be estimated by the Steinmetz equation, $P_{\text{core}} = KV_\text{c}f_s^\alpha B^\beta$ [9, 22, 25]. B is the peak flux density, which is reasonably approximated in the present application by the assumption that it is produced by a sinusoidal current of rms value equal to i_{rms}, therefore allowing the use of manufacturer supplied loss data

Table 4: DAB converter peak and rms inductor currents.

Variable	Converter modes $\mathrm{M2_P}$ and $\mathrm{M2_N}$	Converter modes $\mathrm{M3_P}$ and $\mathrm{M3_N}$
i_{peak}	$\frac{v_{bat}}{4f_sL}(\lvert D_2\rvert(1+d)+(1-D_1-\lvert D_2\rvert)\lvert 1-d\rvert)$	$\frac{v_{bat}}{4f_sL}(\lvert D_2\rvert(1+d)+(1-D_1-\lvert D_2\rvert)\lvert 1-d\rvert)$
i_{rms}	$\frac{\sqrt{3}v_{bat}}{12f_sL}\sqrt{\lvert(2D_1^3d^2-12D_1^2\lvert D_2\rvert d-3D_1^2d^2-8\lvert D_2\rvert^3d+2D_1^3+6D_1^2d+12D_2^2d-3D_1^2+d^2-2d+1)\rvert}$	$\frac{\sqrt{3}v_{bat}}{12f_sL}\sqrt{\lvert(2D_1^3d^2-4D_1^3d-3D_1^2d^2-12D_1D_2^2d-4\lvert D_2\rvert^3d+2D_1^3+12D_2^2d-3D_1^2+d^2-2d+1)\rvert}$

[39] to estimate the material constants K, α and β [40]. The core loss is therefore given by:

$$P_{\mathrm{core}} = KV_{\mathrm{c}}f_s\left(\frac{\sqrt{2}\mu_0N_1i_{\mathrm{rms}}}{l_g}\right)^2, \tag{7}$$

which can be formulated as a constant equivalent resistance

$$R_{\mathrm{eq}} = \frac{2KV_{\mathrm{c}}f_s\mu_0^2N_1^2}{l_g^2}, \tag{8}$$

(= 15.7 mΩ) multiplied by i_{rms}^2.

By considering the average power output and the conduction, switching, copper and core loss expressions, the DAB converter efficiency can be calculated. Efficiency maps for a design DC-link voltage of 700 V, for the cases 1) as D_1 and D_2 vary at constant d values (Fig. 6), and 2) as d and D_2 vary with $D_1 = 0$ (left plot in Fig. 7), are found. In particular, the latter case corresponds to SPS and will later be contrasted against a similar plot of the optimized DPS case.

The Infineon FS150R12KT4 IGBT module is selected for all the switches in both bridges of the DAB converter, as well as for the inverter and rectifier. This module is chosen according to the switched voltage, and the worst case continuous and peak currents in all operating conditions of the vehicle based on the drive cycle range studied. The DC-link design voltage is set at 700 V, and the turns ratio, shown in Table 2, is chosen as the ratio of this DC-link voltage to the battery open circuit voltage (= 320.68 V) such that $d = 1$ while the DC-link voltage is at its design value. This will result in a reduction of hard-switching losses in the DAB converter [38], which can also be seen in Fig. 6; high efficiency of the $d = 1$ case around the $D_2 = 0$ region as compared to low efficiencies of the $d = 0.6$ and $d = 1.2$ cases in the same region.

The DC-DC DAB converter is integrated in the overall vehicle model as a 2-input 2-output component model as shown in Fig. 2. The inputs and outputs of this component are related by the average output power, as given in Table 3, and the total DAB converter power loss given by $P_{\mathrm{totalloss}} = P_{\mathrm{conduction}} + P_{\mathrm{switching}} + P_{\mathrm{copper}} + P_{\mathrm{core}}$. Thus

$$i_{SS} = \begin{cases} \dfrac{P_{\mathrm{out}}}{v_{dc}} & i_{SS} \geq 0 \; (P_{\mathrm{out}} \geq 0) \\ \dfrac{P_{\mathrm{out}} - P_{\mathrm{totalloss}}}{v_{dc}} & i_{SS} < 0 \; (P_{\mathrm{out}} < 0) \end{cases}, \tag{9}$$

and

$$i_{bat} = \begin{cases} \dfrac{P_{\mathrm{out}} + P_{\mathrm{totalloss}}}{v_{bat}} & i_{SS} \geq 0 \; (P_{\mathrm{out}} \geq 0) \\ \dfrac{P_{\mathrm{out}}}{v_{bat}} & i_{SS} < 0 \; (P_{\mathrm{out}} < 0) \end{cases}. \tag{10}$$

The SS power into the DC-link is found by $P_{SS} = i_{SS}v_{dc}$.

3. Control of DC-link Voltage

The paper investigates and compares three control schemes which are detailed in this Section: a) the constant voltage PI control, b) the single phase-shift proportional ratio control, and c) the dual phase-shift proportional ratio control.

3.1. Constant Voltage PI Control

The constant voltage PI control is the conventional control method of the DC-link [25, 29]. Its aim is to keep the DC-link voltage at a constant value. Thus the input of this scheme is the error between a constant reference and the actual DC-link voltage. In response to this, the control adjusts the phase shift ϕ between the gate signals of the LV and HV bridges of the converter, which is equivalent to setting $D_1 = 0$ and adjusting the D_2 phase shift in DPS. The objective is to affect the power provided by the DAB converter, so as to maintain a constant DC-link voltage, despite any variations in the battery voltage. A DC-link voltage reference value equal to the design value of 700 V (at which the devices of all the converters in the powertrain are sized) is chosen in the present work. This value is suitable to enable general vehicle operation while the inverter and rectifier remain in linear modulation. A diagram of the control scheme is shown in Fig. 8.

3.2. Single Phase-Shift Proportional Ratio Control (SPS*)

The basis of the SPS* scheme is the ‘persistent zero voltage switching control’ introduced in [25]. It operates by the implementation of a proportional control law between the voltage conversion ratio and the phase shift ϕ of the gating signals between the two bridges of the converter, as follows:

$$\phi = K_p(1-d), \tag{11}$$

in which K_p is a constant. The manipulated controller variable is therefore ϕ, the same as the PI controller. The control law in (11) corresponds to a diagonal line on the d-ϕ plane passing through the origin ($(d,\phi) = (1,0)$ point), as shown in the left plot in Fig. 7, where D_2 is equivalent to ϕ (at $D_1 = 0$).

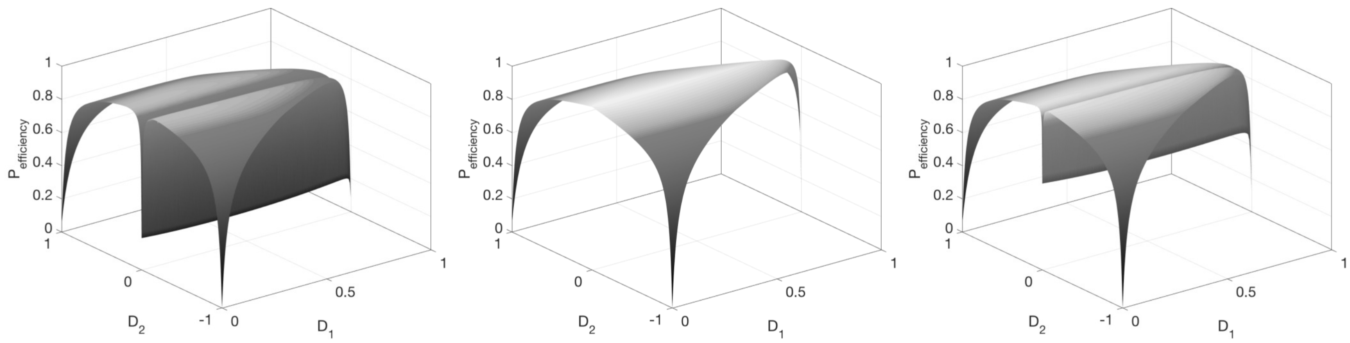

Figure 6: DC-DC converter power efficiency variation with D_1 and D_2 for d = 0.6 (left), d = 1.0 (middle) and d = 1.2 (right).

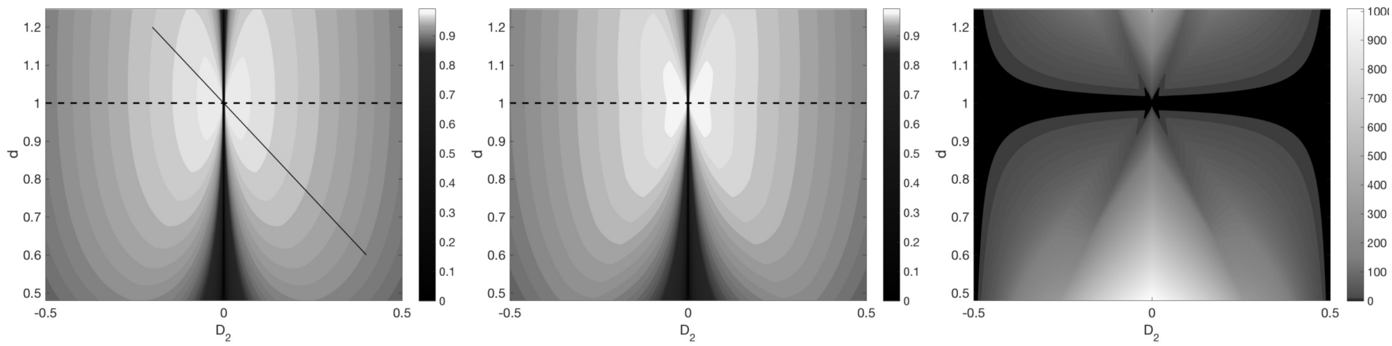

Figure 7: DC-DC converter SPS power efficiency (left), DPS power efficiency (middle) and total power loss difference (right) variation with d and D_2. In the left plot D_1=0 and in the middle plot D_1 is evaluated by the relevant equations in Table 5. The diagonal line in the left plot illustrates diagrammatically the SPS* control law in (11).

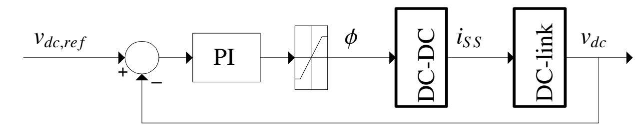

Figure 8: Block diagram of the PI control.

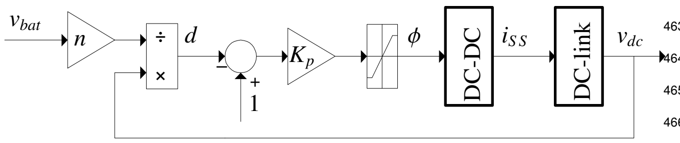

Figure 9: Block diagram showing the SPS* control.

A block diagram of the scheme is shown in Fig. 9. The motivation of this control scheme is: a) to enable stable operation of the DAB converter, since operating points in the reverse-boost and forward-buck regions naturally tend towards the origin, and b) to avoid low efficiency operation at or near $\phi = 0$, $d \neq 1$ regions; see Fig. 6 (at $d \neq 1$ and $D_1 = 0$) and left plot in Fig. 7. K_p corresponds to the negative inverse slope of the line in the d-ϕ plane and further to previous work [25] it is now used as a tuning constant. The objective of tuning K_p is to bend the diagonal line in the left plot in Fig. 7 such that it passes through regions of best efficiency for the operating conditions defined by the given drive cycle.

The SPS* control law, however, introduces constraints on the positive P_{SS} power, additionally to the constraints imposed by the SCS and described in Section 2.1. By setting $D_1 = 0$ and substituting $D_2 = \phi$ in the P_{out} equation for M2P region in Table 3, with d substituted from (11), it can be found that P_{SS} has a cubic dependence with the phase-shift ϕ and has a maximum positive value that depends on K_p and which is not at $\phi = 0.5$ as when d is constant. Simulations of the vehicle model following the drive cycles of interest that will be discussed later in Section 4 show that the battery voltage does not undergo large variations and it remains approximately between 290 V and 360 V, with the lower values in this range associated with the higher power out of the battery. For illustration purposes and to gain insight on the operation and limitations of the SPS* control scheme, the dependence of the maximum P_{SS} value with K_p for an assumed constant value of v_{bat} = 300 V is shown in Fig. 10. It can be

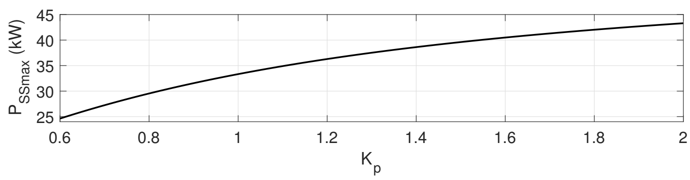

Figure 10: Maximum P_{SS} for a range of K_p values with v_{bat} assumed 300 V.

seen that lower values of K_p place a more stringent constraint on P_{SS} than higher K_p values, which can be even more restrictive than the 42 kW constraint imposed by the SCS.

3.3. Dual Phase-Shift Proportional Ratio Control (DPS*)

DPS operation of the DAB converter offers two controllable variables, D_1 and D_2, rather than the single variable of SPS, to regulate the power flow. As shown in Fig. 5, the maximum converter power is at $(D_1, D_2) = (0, 0.5)$ (or at $(D_1, D_2) = (0, -0.5)$ for negative power). For any other power requirement there is an infinite number of phase-shift pairs (D_1, D_2) that can be selected when operating at some d value. These two degrees of freedom are exploited to introduce a new control scheme described in this Section. The new DPS* control chooses the first degree of freedom D_2 by the same control law as the SPS* scheme of the previous Section:

$$D_2 = K_p(1 - d). \tag{12}$$

Thus it has a similar motivation but it also has the same limitations in the maximum positive P_{SS} as in the SPS* control methodology; see Fig. 10. The second degree of freedom D_1 is determined for any D_2 value such that a certain performance index is optimized to minimize the converter losses for a defined output power. Performance indices such as peak or rms inductor currents, reactive power, or total efficiency have been considered and provided D_2-D_1 trajectories in simple isolated applications in the literature [22, 23, 26, 27]. These performance indices are motivated by the strong dependence of converter losses to these quantities, which can also be seen in (6) and (7) for the rms current. The peak current is chosen as the performance index in the present work to lead to a tractable minimization problem and provide a simple analytic relationship between D_1 and D_2 that can easily be implemented in real-time. It will also be shown in Fig. 11 that minimization of the peak current leads to solutions which are generally close to minimizing the total converter losses (or maximizing its total efficiency). To optimize the peak current for a specified power P_0, the Lagrangian objective function is constructed as follows:

$$L_a(D_1, D_2, \lambda) = i_{\text{peak}}(D_1, D_2) + \lambda(P_{\text{out}}(D_1, D_2) - P_0), \tag{13}$$

in which only quantities in modes M2_N, M3_N, M2_P and M3_P are involved. The expressions for i_{peak} and P_{out} for these modes are given in Tables 4 and 3 respectively. The minimum value occurs when $\frac{\partial L_a}{\partial D_1} = 0$, $\frac{\partial L_a}{\partial D_2} = 0$ and $\frac{\partial L_a}{\partial \lambda} = P_{\text{out}}(D_1, D_2) - P_0 = 0$, which lead to the solutions $D_1 = f(D_2, d)$ shown in Table 5. These solutions are piecewise linear trajectories on the D_2-D_1 plane not exceeding $|D_2| = 0.5$ in any case, as shown for two exemplary d values in Fig. 11. The numerical solutions that maximize the overall DAB converter efficiency for each of the d values are also shown in the same figure for comparison purposes.

Table 5: D_1 as a function of D_2 and d to minimize peak current i_{peak}.

Mode	Equation
M2_P & M2_N, $d < 1$	$D_1 = \frac{1-d}{d}(-\lvert D_2\rvert + 0.5)$
M2_P & M2_N, $d \geq 1$	$D_1 = (d-1)(-\lvert D_2\rvert + 0.5)$
M3_P & M3_N, $d < 1$	$D_1 = -\frac{1+d}{1-d}\lvert D_2\rvert + 1$
M3_P & M3_N, $d \geq 1$	$D_1 = -\frac{d+1}{d-1}\lvert D_2\rvert + 1$

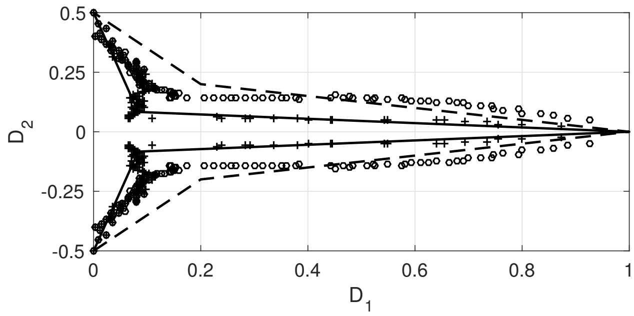

Figure 11: D_2-D_1 relationship to minimize peak current i_{peak}, for $d = 0.6$ (dashed line) and $d = 1.2$ (solid line). The D_2-D_1 relationship that maximizes the overall DAB converter efficiency, found numerically, is also shown for $d = 0.6$ (circles) and for $d = 1.2$ (crosses).

The ultimate step in setting up the DPS* control scheme is to combine the control law introduced in (12) and the optimal trajectories in Table 5 to eliminate d and obtain a relationship between the controllable variables D_1 and D_2 only. The only feasible solutions to this problem are found to describe trajectories that are entirely in M2_P and M2_N, as follows:

$$D_1 = \begin{cases} \dfrac{D_2(-D_2 + 0.5)}{K_p - D_2} & D_2 \geq 0,\ d < 1 \\[2ex] \dfrac{-D_2(D_2 + 0.5)}{K_p} & D_2 < 0,\ d \geq 1 \end{cases}, \tag{14}$$

subject to $K_p \geq 0.5$. Thus, with this control, modes M3_P and M3_N are not entered. A block diagram of the overall control scheme is shown in Fig. 12. It is clear that when $f(D_2)$ is set to zero, this scheme reduces to the SPS* control, shown in Fig. 9. The constant K_p remains a tuning parameter as in SPS* control.

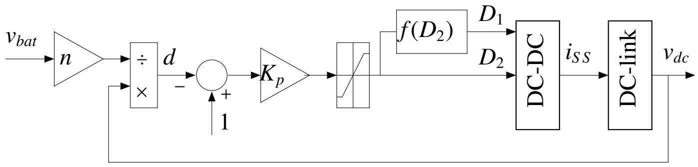

Figure 12: Block diagram of DPS* control. $f(D_2)$ corresponds to Equation (14).

Exemplary cases of trajectories and the influence of K_p on the trajectories are illustrated in Fig. 13. The motivation for tuning K_p is equivalent to SPS* control: to bend the line on the d-D_2 plane defined by the control law in (12) so that it intersects regions of high efficiency. Such regions can be seen in the middle plot of Figure 7 that shows the variation of efficiency on the d-D_2 plane and in which at every point D_1 is evaluated by the relevant equations in Table 5. In order to provide more clarity on the efficiency improvement of DPS* with respect to SPS* control, the right plot in Fig. 7 illustrates the difference of the total power loss between SPS and DPS control cases on the

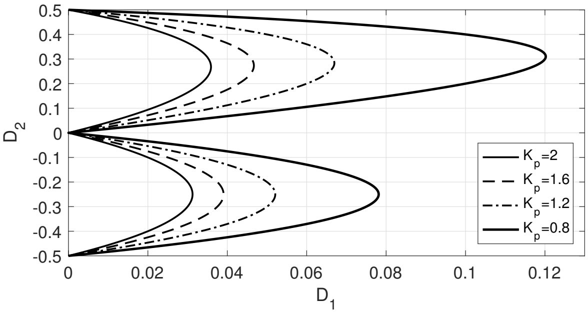

Figure 13: Optimal D_2-D_1 trajectory for various values of K_p.

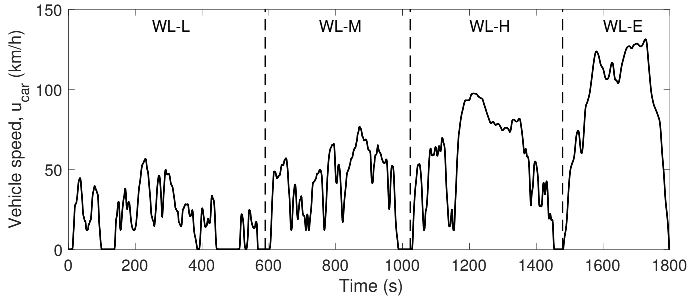

Figure 14: WLTP speed profile, with the four constituent drive cycles delimited (WL-L, WL-M, WL-H and WL-E).

d-D_2 plane. These power losses are essentially the quantities that have been used to calculate the efficiencies of the SPS and DPS schemes respectively in the left and middle plots in the same Figure. As it can be seen, in all regions the SPS losses are at least the same (black color) or higher (dark/light gray, white color). It is clear that the line locus defined by the control law in (12) should be bent by selecting K_p such that it crosses the dark gray and some part of the light gray regions. Further bending into the light-gray/white regions is not desirable because, even though the DPS* control manifests much smaller losses than SPS* control, the overall DAB converter efficiency in those regions is not as good as in the regions where the dark gray color dominates; see middle plot in Fig. 7.

4. Simulation Results

The performance and operation of the three voltage control strategies presented are assessed and compared in this Section. This is done by simulation of the vehicle model described, with the Thermostat and Power Follower SCSs.

4.1. Drive cycles

Each of the four component drive cycles of the worldwide harmonized light vehicle test procedures (WLTP) are simulated: WL-L (low speed), WL-M (medium speed), WL-H (high speed) and WL-E (extra-high speed). These profiles have been developed in recent years by the United Nations to reflect more accurately real-world driving conditions as compared to older drive cycles, and to provide a global standard for the determination of emissions, fuel consumption and electric range of light-duty vehicles [41]. The drive cycles are shown in Fig. 14, while Table 6 provides some of their characteristic details (P_{PL} load characteristics are specific to vehicle design). In order to enable the investigation of behaviour manifested over long enough time scales, multiple iterations of each drive cycle are simulated in each case: WL-L × 8, WL-M × 8, WL-H × 4, and WL-E × 4.

Table 6: WLTP drive profile characteristics.

	Units	WL-L	WL-M	WL-H	WL-E
Duration	s	589	433	455	323
Stationary duration	s	156	48	31	7
Distance	m	3095	4756	7158	8254
Maximum speed	km/h	56.5	76.6	97.4	131.3
Ave. speed (no stops)	km/h	25.7	44.5	60.8	94.0
Average speed	km/h	18.9	39.5	56.6	92.0
Min. acceleration	m/s^2	-1.47	-1.49	-1.49	-1.21
Max. acceleration	m/s^2	1.47	1.57	1.58	1.03
Maximum P_{PL} load	kW	25.84	36.12	41.71	50.37
Average P_{PL} load	kW	1.95	4.53	7.38	17.33

4.2. Equivalent fuel consumption

The DAB converter is part of and interacts with the other components of the powertrain whose operation and efficiency can be influenced by variations of the DC-link voltage effected by the voltage control schemes. For example, the modulation indexes and consequently the efficiency of the inverter and rectifier are changed when the DC-link voltage changes, while it is also possible for the number of engine turn-on occurrences by the start-stop system to be similarly affected. Therefore, as described in Section 3, the controllers are set up on the basis of minimizing the DAB converter losses but their parameters are tuned by simulations to provide a combined benefit for all the powertrain components realized in terms of minimizing fuel consumption. These two minimization objectives are generally but not always compatible and sometimes some DAB converter efficiency needs to be sacrificed for the purpose of improving the overall powertrain efficiency.

In order to make the evaluation of fuel economy appropriate, the concept of equivalent fuel consumption (m_{EFC}) is applied. It enables the overall fuel economy to be compared by accounting for the actual fuel consumption in the ICE and also the deviation of the battery final SOC from its initial value. Such a fuel consumption to SOC equivalence has been studied in the literature by various analytical methods. In the present work, the line-chart methodology described in [42] is employed which is also a natural extension of the popular equivalent consumption minimization strategy (ECMS) [43]. The line-chart methodology involves identifying the discharging and charging equivalence factors, s_{d} and s_{c}, that respectively translate SS energy discharged or charged into an associated amount of fuel consumed or stored. This is done by using simulation data, such that

$$m_{\mathrm{EFC}} = m_f + s_{\mathrm{d}} \cdot \Delta soc \frac{Q_{\max} V_{\mathrm{b,OC}}}{Q_{\mathrm{LHV}}} \quad \Delta soc \geq 0,$$

$$m_{\mathrm{EFC}} = m_f + s_{\mathrm{c}} \cdot \Delta soc \frac{Q_{\max} V_{\mathrm{b,OC}}}{Q_{\mathrm{LHV}}} \quad \Delta soc < 0, \tag{15}$$

in which m_f is the ICE fuel consumption, $\Delta soc = SOC_{\mathrm{initial}} - SOC_{\mathrm{final}}$, $Q_{\max}$ is the battery capacity, $V_{\mathrm{b,OC}}$ is the battery open-circuit voltage and Q_{LHV} is the lower heating value of the fuel. The equivalence factors are required to be identified for each drive cycle, with the present work utilizing values for these factors identified for the basis model in [28].

4.3. Tuning

The controllers described in Section 3 are tuned by simulations, primarily to optimize the fuel economy but also to achieve stable operation of the DAB converter and the overall powertrain in the presence of many system constraints and nonlinearities. One such significant nonlinearity in the control exists near $D_2 = 0.5$ and $D_2 = -0.5$, where the power provided by the DAB converter per D_2 changes sign on either side of these operating points. The same D_2 points also correspond to the operational limit boundaries of the range $|D_2| \leq 0.5$ ($|\phi| \leq 0.5$ for SPS) outside which it is very inefficient to operate the DAB converter. In order to alleviate both the nonlinearity and inefficiency, the value of the D_2 (ϕ in SPS) control input is hard-constrained to remain in the range mentioned. However, if at any time D_2 reaches the limits, the control saturates and the overall system may behave inefficiently and even unpredictably. Healthy and stable operation of the DC-DC converter and powertrain is anticipated when D_2 remains away from the limits and relatively near the origin ($D_2 = 0$), where the variation of P_{out} with D_2 is approximately linear. This can be achieved by the choice of design parameters, such as the leakage/auxiliary inductance and DAB converter switching frequency, to obtain a high enough converter peak power for the range of power values required by the followed drive cycles, or by tuning, as will be described. Indeed, the best approach, which is also followed in this paper, is to use both of these options and obtain a well tuned system without over-specifying the design.

The PI controller is easy to tune by trial and error to enable the DC-link voltage to remain close to the reference value of 700 V without requiring large D_2 values. The proportional and integral gains found to be suitable are $K_{p,\mathrm{PI}} = 0.1$ and $K_{i,\mathrm{PI}} = 0.05$ respectively for all drive cycles.

The tuning of SPS* and DPS* controllers is confounded by their interaction with the supervisory control system. The SCSs parameters have been obtained by a separate tuning exercise conducted with the basis vehicle model [28]. Each SCS takes as input the SOC of the battery and demanded power P_{PL} and outputs the reference PS power P_{PSref}. The power from the DC-DC converter (P_{SS}) is injected into/out of the DC-link because of the dynamics of the DC-link and its voltage control, to match the power difference between P_{PL} and P_{PS}. The P_{PL} input to the SCS is calculated by multiplying the inverter input current i_{PL} by the DC-link voltage. However, due to the dynamic changes in the DC-link voltage by the SPS* and DPS* controllers, complex nonlinear unstable system dynamics arise involving the interaction of the DC-DC converter controller, the SCS, various saturating constraints such as for the D_2, the modulation indexes of the inverter and rectifier and so on. To address this underlying deleterious dynamic coupling of system components, instead of using the actual DC-link voltage value to compute the P_{PL} input to the SCS, a constant 'reference' value V_{dcref} is used. This parameter is then identified by tuning, together with K_p, using simulations results.

Simulations have been conducted for all combinations of drive cycles, SPS* and DPS* control schemes, and TCS and PFC SCSs. The simulations have been used to iteratively tune K_p and V_{dcref} by a simple search method to minimize the equivalent fuel mass m_{EFC}, as shown in Table 7. The loci of d-D_2 in each simulation case are shown in Figure 15, superimposed on the efficiency and power difference diagrams. The straight lines passing through the origin correspond to the SPS* and DPS* simulations, with their slope given by $-1/K_p$ (see (11) and (12)). The jagged lines passing around the origin and having a positive average slope correspond to simulations with a PI-controlled DAB converter. It can be seen that all the lines stay away from the D_2 limits of ± 0.5 with the lines extending more into the positive D_2 side. This is due to higher magnitudes of positive (battery discharging) P_{SS} values than negative (charging) ones being possible/allowed by the design/SCS, as described in Section 2.1. The SPS* and DPS* lines pass through the origin and therefore avoid the low efficiency regions at $d \neq 1$ when D_2 changes sign. However, this is not the case with the PI control scheme in which the DAB converter is often operated at inefficient points around the origin. Excluding the WL-E case, the slopes of the SPS* and DPS* lines become steeper (K_p reduces) as the vehicle is operated with the PFC SCS in a higher-speed drive cycle. The opposite can be said when the vehicle is operated with the TCS SCS. There is also a correlation between the V_{dcref} tuning variable value and the maximum value of D_2 reached in each drive cycle case; lower V_{dcref} values are associated with larger D_2 maximum values. For example, the line which extends to the largest D_2 value corresponds to WL-E being followed with PFC as the SCS, and for which $V_{dcref} = 540$, which is the lowest V_{dcref} amongst all cases. The K_p and V_{dfref} values for SPS* are tuned individually as compared to those for DPS* but they result in similar and often identical values. In the DPS* case the lines can be seen to pass through the dark

Table 7: SPS and DPS control parameters for WL-L, WL-M, WL-H, and WL-E drive cycles.

		$\mathrm{SPS}^*_{\mathrm{TCS}}$	$\mathrm{DPS}^*_{\mathrm{TCS}}$	$\mathrm{SPS}^*_{\mathrm{PFC}}$	$\mathrm{DPS}^*_{\mathrm{PFC}}$
K_p	WL-L	1.4	0.9	1.0	0.9
K_p	WL-M	1.6	1.6	0.8	0.85
K_p	WL-H	1.9	1.8	0.65	0.7
K_p	WL-E	0.9	0.9	0.7	0.75
V_{dcref}	WL-L	660	680	720	720
V_{dcref}	WL-M	860	860	720	730
V_{dcref}	WL-H	920	920	600	600
V_{dcref}	WL-E	800	800	540	540

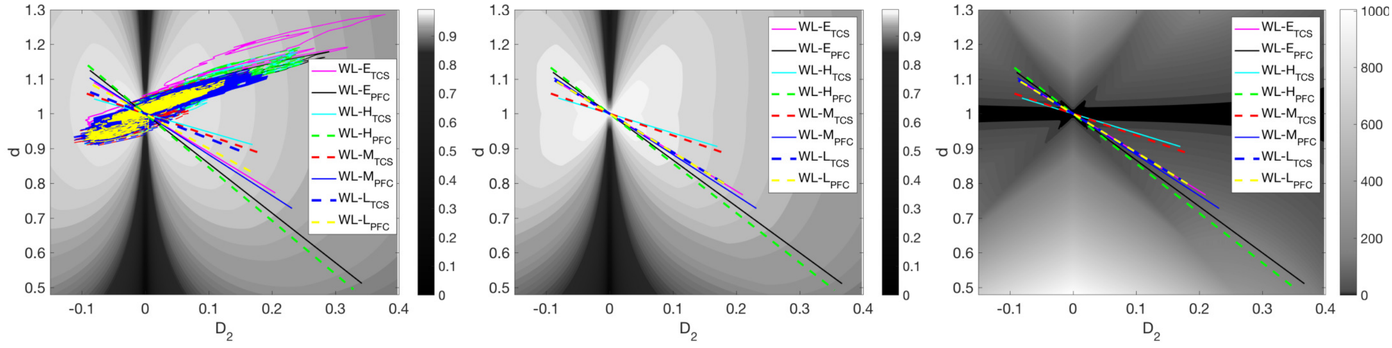

Figure 15: DC-DC converter single-phase power efficiency (left), dual-phase power efficiency (middle) and total power loss difference (right) variation with d and D_2 (as in Fig. 7), superimposed with loci (traces) of d against D_2 for various simulation cases. The traces belong to three groups of simulation cases, employing the PI, SPS*, and DPS* voltage control schemes respectively, with each group including simulation cases for all combinations of drive cycles (WL-L, WL-M, WL-H, and WL-E) and supervisory control schemes (TCS and PFC). The PI simulation group is superimposed on the left plot (jagged lines), the SPS* group is superimposed also on the left plot (straight lines), and the DPS* group is superimposed on the middle and right plots (also straight lines).

gray and some part of the light gray regions in the total power loss difference diagram, as has been the aim of tuning, indicating the savings in energy loss of the DPS* control scheme over the SPS* scheme. The actual D_2-D_1 loci for each simulation with the DPS* control are shown in Fig. 16 demonstrating the respective optimal trajectories followed.

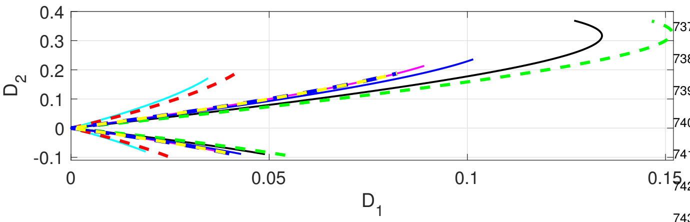

Figure 16: DPS* D_2 against D_1 simulation results for all drive cycles. The line styles are the same as in Fig. 15.

4.4. Power profiles

Further insight into the operation of the designed control schemes is obtained by looking into simulation time histories. Figures 17 to 20 illustrate drive cycle, P_{PL}, P_{PS}, and P_{SS} time histories for selected drive cycle iterations. Only one P_{PL} time history is shown in the diagrams since it depends essentially on the road load imposed by the drive cycle and not on the SCS or voltage control scheme employed, due to the series architecture of the powertrain. Sometimes for each SCS case, the time histories with SPS* and DPS* controls differ by a small enough amount that is not discernible at the scale of the illustrated diagrams, hence only one of the two cases is shown as a representation of both cases. As expected, when the vehicle is accelerating, positive P_{PL} spikes occur and conversely when the vehicle decelerates, P_{PL} reaches negative values indicating regenerative braking is taking place. P_{PS} and P_{SS} cumulatively serve the P_{PL} load but they do so by a pattern which depends on the SCS and voltage control scheme being employed. The pattern of the PS and SS power profiles is also influenced by the drive cycle being followed. This can be observed in Fig. 17 in which the PS is mostly switched off and the power is provided mostly from the SS, due to the low power requirements of the WL-L drive cycle. P_{PS} is non-zero only at two approximately 500 s long intervals at approximately 1000 s and 3700 s into the simulation in all control cases. In contrast, in the case of WL-E in Fig. 20 that has the highest power requirements, the PS is switched on almost continuously (since SS power alone is not enough) generally providing power $P_{PS\,opt} = 19.8$ kW in the case of TCS or following the load power P_{PL} with $P_{min} = 16.8$ kW in the case of PFC. For the other two drive cycles (WL-M and WL-H in Figs. 18 and 19 respectively), which pose intermediate power requirements, the pattern of behaviour is between the two extreme cases mentioned, with PS on for longer intervals than for the WL-L and not as long as for WL-E. However, in these intermediate drive cycles there are also more interactions of the SCS with the variations of the DC-link voltage by the SPS* and DPS* control (but not the PI control). The result is more frequent ICE switching events evidenced by the presence of a number of short duration spikes in the P_{PS} time histories, with this being more prevalent in the case of TCS.

P_{SS} remains mostly above the negative power limit of the SS imposed by the SCS (−21 kW) in all DC-link voltage control schemes. Exceptions are some time intervals in which there are very small violations due to exception rules existing in the implementation of the SCSs to account for limit operation. In the case of PI control schemes, P_{SS} remains below the positive P_{SS} limit dictated by the SCS (42 kW). However, in the SPS* and DPS* control cases the more restrictive positive P_{SS} constraint imposed by the associated control laws, described in Section 3.2 and Fig. 10, dominates, especially in the cases where K_p has a lower value. Examples of this are the PFC cases with both SPS* and DPS* control for all drive cycles, and the TCS cases with SPS* and DPS* control for WL-E.

4.5. DC-link voltage and modulation indexes

Figures 17 to 20 also depict simulation time histories for v_{dc}, inverter modulation index (M_{inv}) and rectifier modulation index (M_{rect}). It is clear that there is a strong correlation between v_{dc} and P_{SS} in all SPS* and DPS* control cases for all drive cycles; as P_{SS} increases above (decreases below) zero, v_{dc} de-

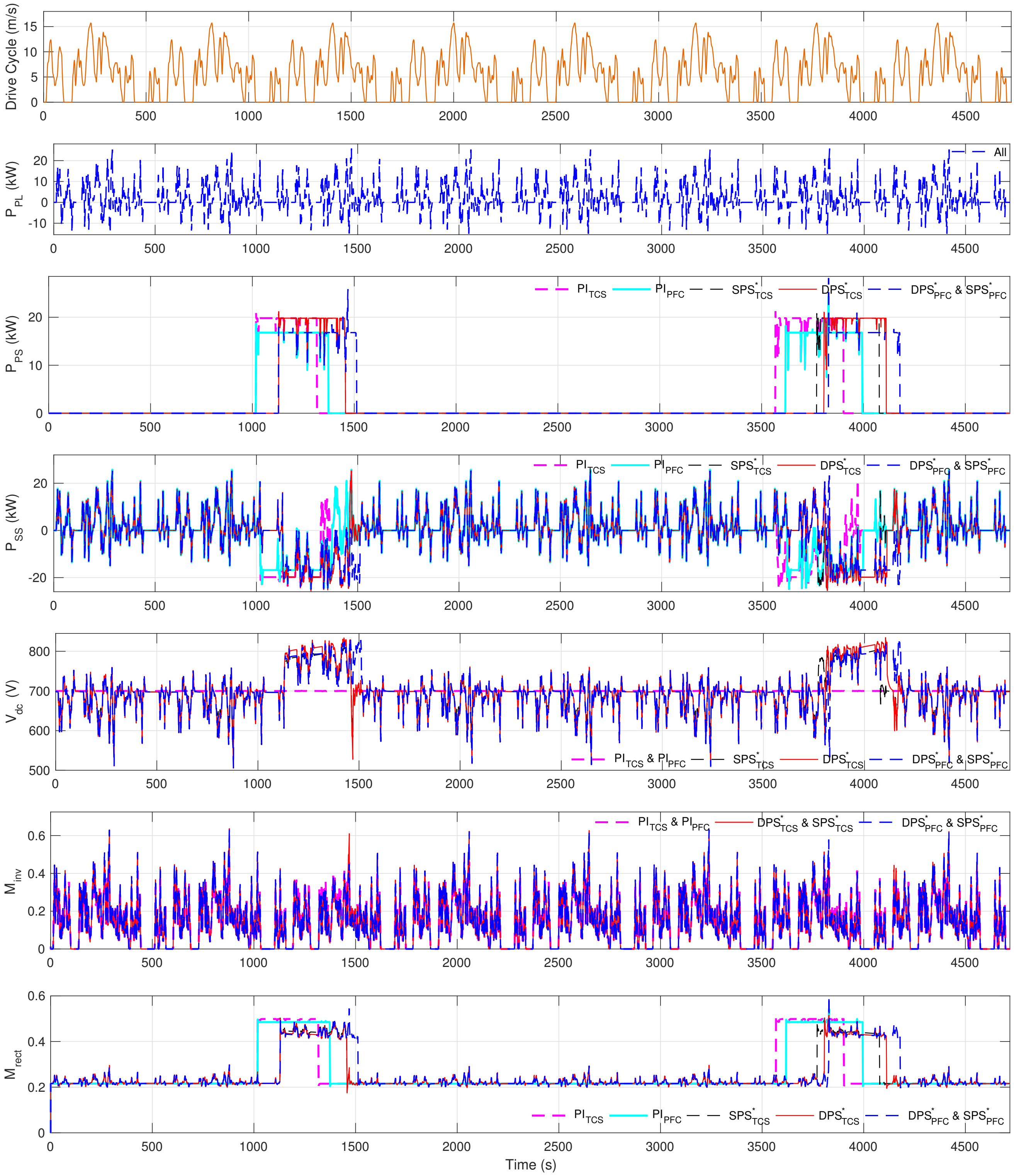

Figure 17: Simulation results for WL-L drive cycle. All of the 8 drive cycle iterations are shown.

creases below (increases above) 700 V. This is a consequence of the SPS* and DPS* control laws in (11) and (12) respectively, which impose an almost linear and with negative slope dependence of the respective phase-shift variable to v_{dc}, since v_{bat} variation is small. As argued in Section 3.2, P_{SS} is then essentially cubically dependent on phase-shift ϕ (or D_2 for DPS*). The large dips in v_{dc}, which are more pronounced in the WL-H and WL-E simulation results with the PFC, are caused by positive less pronounced spikes in P_{SS} that have reached their K_p-dependent limit value, and which result from the P_{PL} requirements during acceleration phases of the drive cycles. At the same time as when v_{dc} falls sharply, M_{inv} rises sharply to-

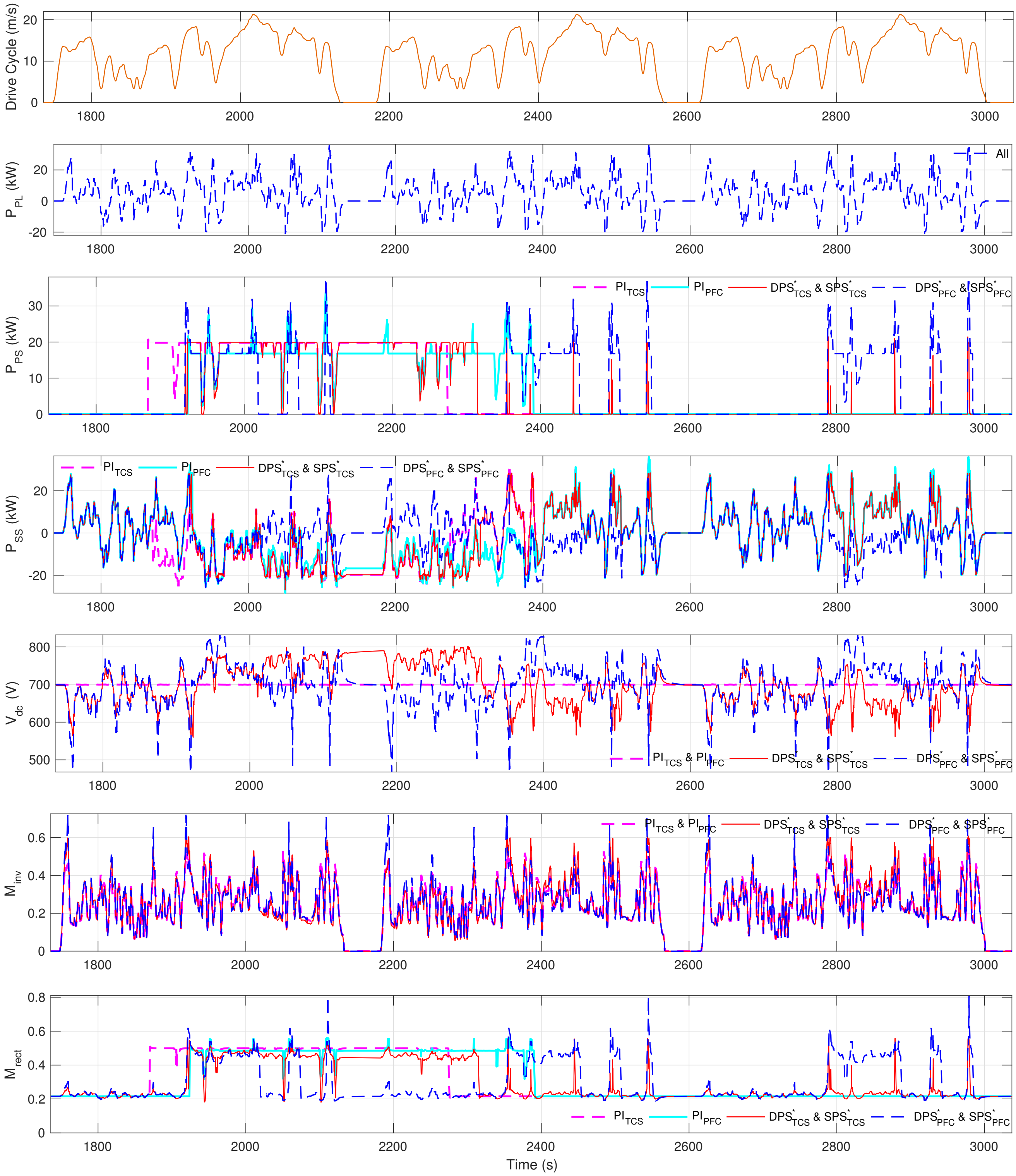

Figure 18: Simulation results for WL-M drive cycle. Drive cycle iterations 5-7 are shown.

wards the value of 1 and in some instances, such as in WL-H and WL-E, it saturates at 1, with overmodulation prevented by the imposed constraint (see Section 2.3). The simulation results also show that M_{rect} varies by a pattern which is similar to P_{PS} and despite v_{dc} varies significantly, M_{rect} remains below the value of 0.9 in all simulation cases.

4.6. *Losses and fuel economy*

The overall fuel economy comparison (Δ_{fuel}) is summarized in Table 8 together with details of the number of engine start-stop events (N_{SS}), and inverter (Δ_{inv}), rectifier (Δ_{rect}) and DC-DC converter (Δ_{dcdc}) losses percentage increase, for all drive cycles, and supervisory and voltage control schemes. All the Δ

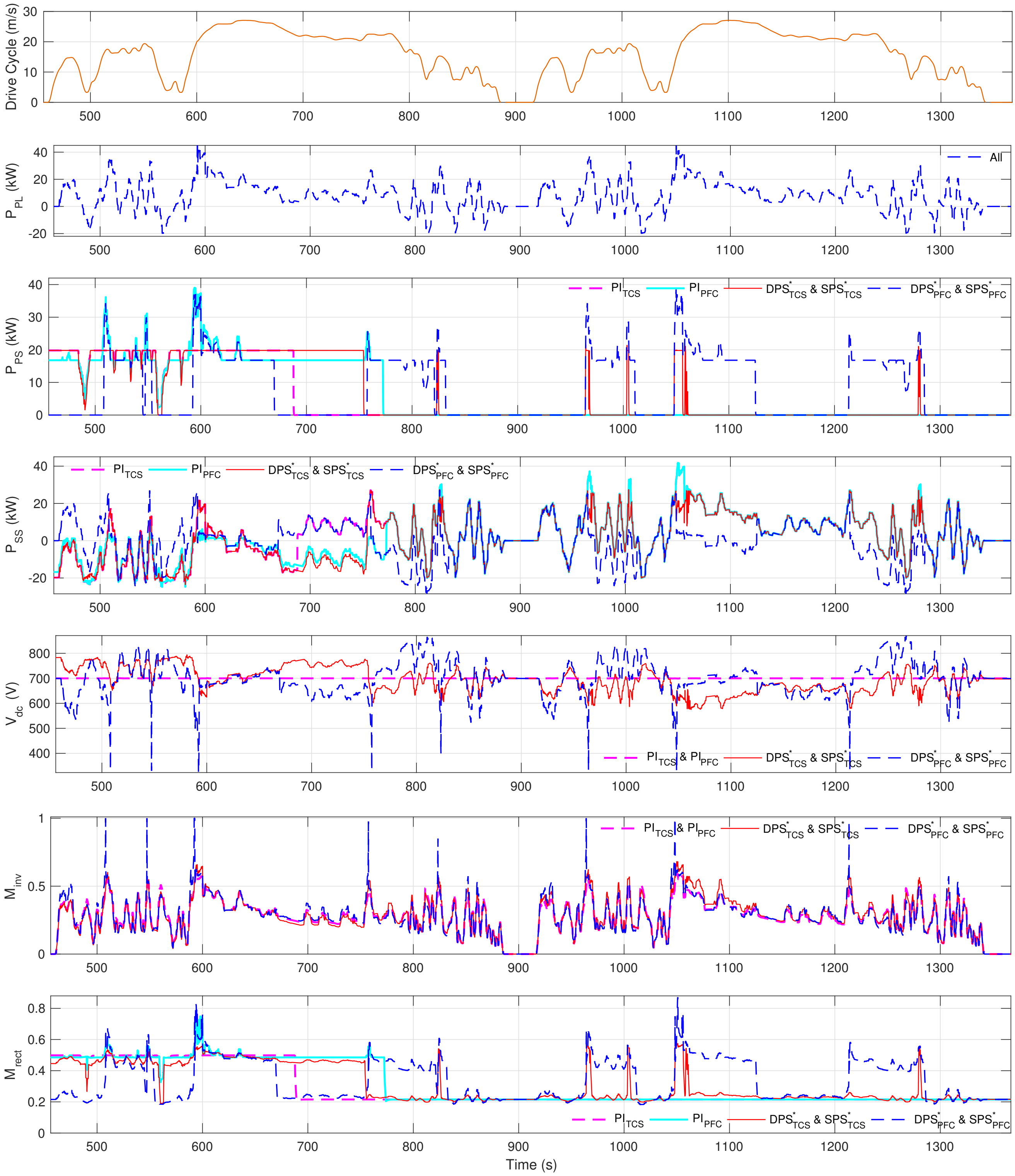

Figure 19: Simulation results for WL-H drive cycle. Drive cycle iterations 2-3 are shown.

variables represent percentage increase in losses or fuel compared to the rightmost column ($\mathrm{DPS}^*_{\mathrm{PFC}}$) entries which are all zero. The numbers in parentheses represent the percentage increase in losses or fuel compared to the $\mathrm{DPS}^*_{\mathrm{TCS}}$ entries in the middle column which are also all zero. The fuel quantities represent equivalent fuel consumption mass, m_{EFC}.

When the N_{SS} of the SPS* and DPS* control schemes is compared to the PI N_{SS} it becomes clear that the variable DC-link voltage encourages start-stop events, which are associated with a higher fuel penalty. This is obvious in the middle speed range drive cycles, such as WL-M and WL-H, during which there is a higher degree of interaction between the system components

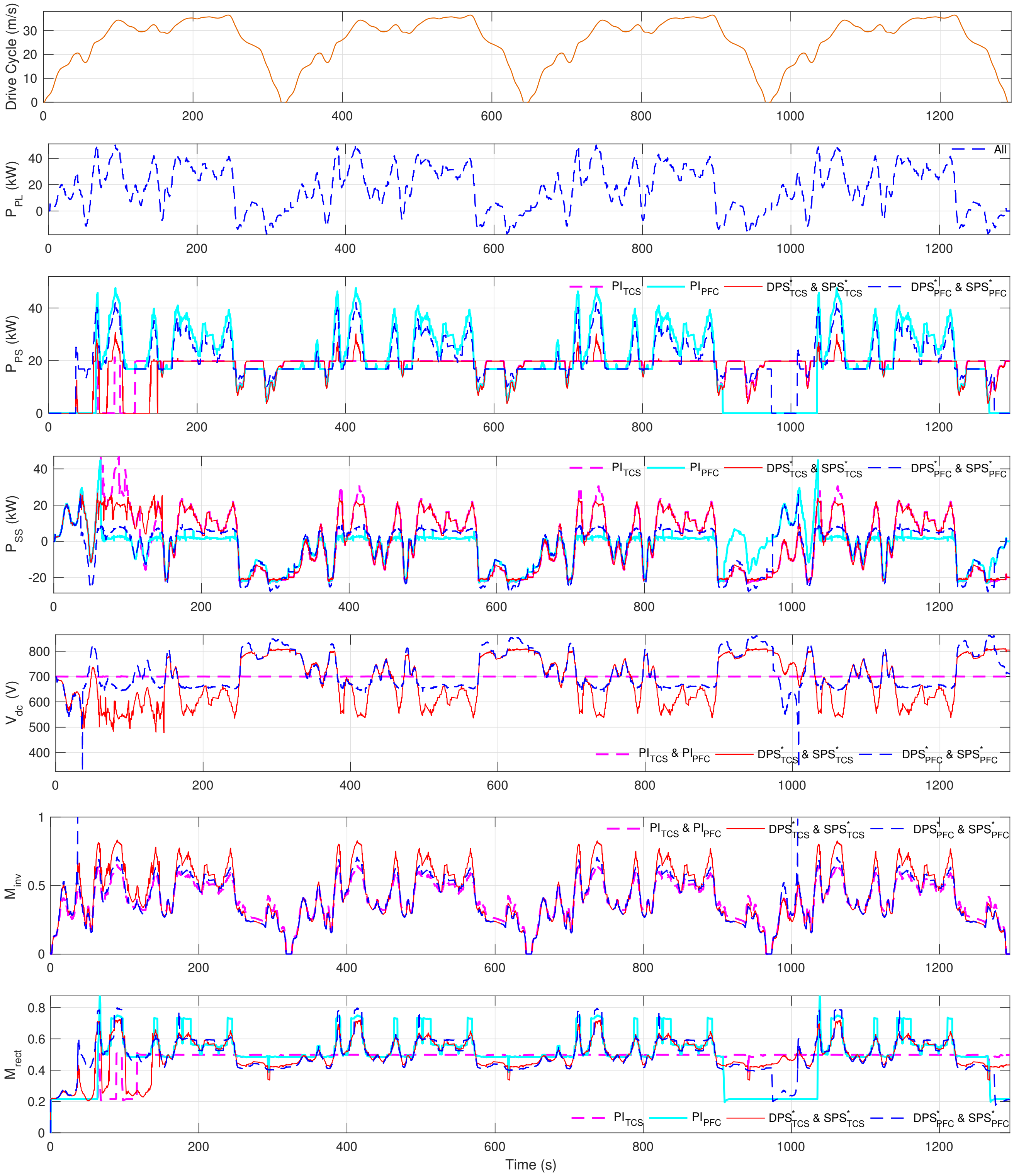

Figure 20: Simulation results for WL-E drive cycle. All of the 4 drive cycle iterations are shown.

and the SCS. However, the low power requirements of WL-L prevent such strong system interactions and there is the same low number of engine start-stop occurrences as with the PI schemes. Although WL-E SPS^*_{TCS} and DPS^*_{TCS} exhibit a high N_{SS}, this is due to the high frequency transient dynamics within the first 150 s of the simulation (see P_{SS} in Fig. 20) and do not persist further into the drive cycle. Indicatively, WL-E SPS^*_{PFC} and DPS^*_{PFC} do not exhibit the same high frequency dynamics at the beginning of the simulation and their N_{SS} is extremely low, since the drive cycle high power requirements essentially lead to uninterrupted, non high frequency transient, utilization of the PS.

The loss in efficiency suffered by the SPS* and DPS* control schemes because of the high N_{SS} is more than covered by improvements in the efficiency of the inverter, rectifier and DC-DC converter compared to the PI schemes. This is clearly seen by observing the numbers in parentheses, corresponding to TCS cases, in which except in one case (Δ_{rect} in WL-L PI_{TCS}) the PI scheme produces higher losses in all converters, reaching as high as 7.38% (inverter), 7.59% (rectifier) and 18.53% (DC-DC converter) more losses than the DPS^*_{TCS} scheme. Consequently, significant fuel savings are obtained by the SPS* and DPS* control schemes in those cases, with the m_{EFC} of the PI-controlled powertrain being up to 3.54% worse than the corresponding DPS* scheme. Similar efficiency conclusions can be drawn by examining the results in the last three columns, corresponding to PFC schemes. However, the picture is slightly more confused since in some cases the PI scheme results in lower losses than the voltage control schemes, such as for the rectifier losses for all drive cycles. Worthy of note is the 16.03% less losses in the DC-DC converter than those with the corresponding DPS* scheme, for WL-E. Even though this is a surprising result at a first glance, closer inspection of the DC-DC converter operation for this case in Fig. 20 provides a plausible explanation. When the PI_{PFC} scheme is used, except from regenerative braking, P_{PL} is matched almost entirely by the PS. The power flow though the DAB converter, P_{SS}, is almost constant and much lower than the corresponding power flow in other control cases. Hence, it suffers lower losses even though its efficiency is worse. Despite the mixed results of loss percentage improvements in the three converters, the fuel economy, which was the objective of tuning the controls, has been successfully improved by employing SPS* and DPS* voltage control, reaching an m_{EFC} improvement of 3.79% in the WL-M drive cycle.

It is more than evident from the tabular results that when the DPS* control method is employed the fuel economy is always better than with the SPS* control in each SCS case. There appears to be a trend of larger improvement with lower speed driving, with the highest improvement in the PFC category being 0.46% and in the TCS category being 0.36%, both for the WL-L drive cycle. Even though the losses in all components together should be considered to interpret the resulting fuel consumption, it is obvious that the DPS* control compared to SPS* control achieves significant reductions in the DC-DC converter losses in all SCS and drive cycle cases, approaching 10% and 8% in the PFC and TCS cases respectively. This result is consistent with the primary function DPS* control was designed to perform. The corresponding benefits are accrued by persistent efficiency improvement throughout any drive cycle and SCS, as shown in Fig. 21.

Finally, a comparison is made between the results of TCS and PFC. The DPS^*_{TCS} column includes the best fuel economy results in the TCS category, while the DPS^*_{PFC} represents the best fuel economy in the PFC category. Once these two columns are compared it becomes clear that TCS is more efficient in equivalent fuel consumption by 0.5% than PFC in the WL-L drive cycle, while the reverse is true for all higher speed drive cycles, with TCS up to 2.45% worse than PFC.

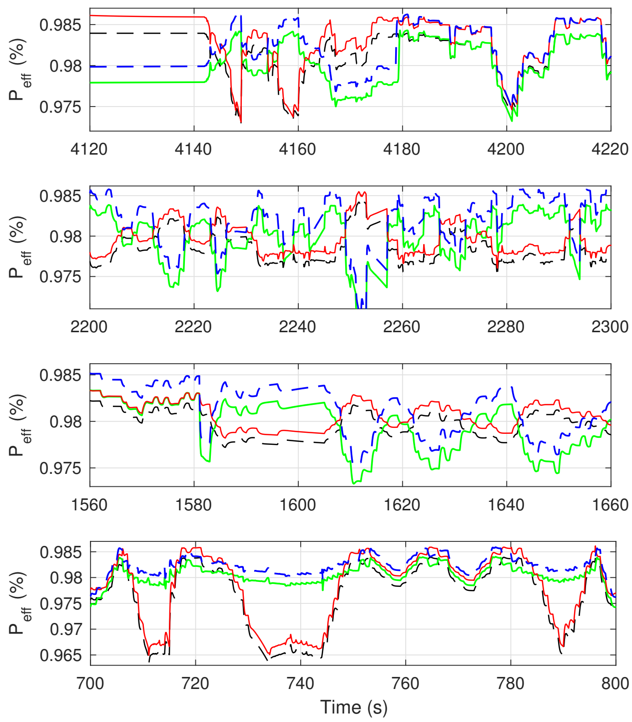

Figure 21: DC-DC converter power efficiency simulation result snapshots for WL-L, WL-M, WL-H and WL-E (top to bottom) drive cycles for SPS^*_{TCS} (black dashed), SPS^*_{PFC} (green solid), DPS^*_{TCS} (red solid) and DPS^*_{PFC} (blue dashed) control schemes.

5. Conclusion

The fuel economy of series HEVs is shown to improve by dynamic variation of the voltage of the DC-link that joins the powertrain converters. The variation is achieved by controlling the power flow of the DAB DC-DC converter that integrates the energy storage device with the DC-link. DC-DC converter single-phase-shift proportional voltage conversion ratio and dual-phase-shift control methodologies significantly outperform constant voltage control, in terms of DC-DC converter efficiency but also overall powertrain system efficiency, following tuning of the control parameters. The benefits are measured as an equivalent fuel consumption reduction, accounting both for real fuel and battery usage. The improvements are obtained for a large range of driving conditions, covering low to very high speed driving. Two popular powertrain supervisory control algorithms are involved in this investigation and the trends in the improvements by the voltage controls are further shown not to be very sensitive to these algorithms. Nonetheless, co-design and co-tuning of the voltage and supervisory controls offers a path for further efficiency improvements, and it is the subject of future investigations.

Despite the significant fuel economy of the single phase-shift control method, this is universally exceeded by the dual phase-shift control by a measurable margin, which is largest for driving in an urban, low speed, environment (reaching 0.46%). The dual phase-shift control method remarkably offers persistent DC-DC converter efficiency improvements that approach 10% over the single phase-shift control, and fuel economy im-

Table 8: Engine start-stop system number of turn-on occurrences (N_{SS}), converter loss percentage increase (Δ_{inv}, Δ_{rect}, and Δ_{dcdc}) and equivalent fuel percentage increase (Δ_{fuel}) results, for all cases of drive cycles, SCSs and voltage control schemes. The results of equivalent fuel percentage increase of the SPS* scheme as compared to the DPS* scheme, for each of the TCS and PFC supervisory control schemes, are shaded.

	Drive cycle	PI_{TCS}	SPS^*_{TCS}	DPS^*_{TCS}	PI_{PFC}	SPS^*_{PFC}	DPS^*_{PFC}
N_{SS}	WL-L	2	2	2	2	2	2
N_{SS}	WL-M	3	74	75	3	24	24
N_{SS}	WL-H	2	35	37	2	11	12
N_{SS}	WL-E	3	43	46	2	2	2
Δ_{inv}	WL-L	(3.14) 3.17	(0.81) 0.84	(0) 0.03	3.17	0.27	0
Δ_{inv}	WL-M	(2.74) 0.83	(0.02) −1.84	(0) −1.86	0.83	−0.07	0
Δ_{inv}	WL-H	(2.11) 1.00	(0.06) −1.03	(0) −1.09	1.00	−0.01	0
Δ_{inv}	WL-E	(7.38) 2.06	(0.08) −4.88	(0) −4.95	2.06	−0.08	0
Δ_{rect}	WL-L	(−3.47) −3.45	(0.36) 0.39	(0) 0.02	−3.19	0.40	0
Δ_{rect}	WL-M	(5.38) 1.87	(0.14) −3.20	(0) −3.33	−3.32	0.28	0
Δ_{rect}	WL-H	(7.59) 2.41	(0.04) −4.78	(0) −4.81	−8.43	0.2	0
Δ_{rect}	WL-E	(2.31) −9.6	(0.05) −11.6	(0)−11.64	−6.14	0.03	0
Δ_{dcdc}	WL-L	(10.88) 14.31	(6.69) 9.99	(0) 3.09	10.72	8.80	0
Δ_{dcdc}	WL-M	(9.9) 65.82	(4.9) 58.26	(0) 50.88	55.78	9.82	0
Δ_{dcdc}	WL-H	(18.53) 69.18	(4.51) 49.17	(0) 42.74	47.94	8.03	0
Δ_{dcdc}	WL-E	(13.82) 90.89	(7.8) 80.78	(0) 67.70	−16.03	9.09	0
Δ_{fuel}	WL-L	(0.60) 0.10	(0.36) −0.14	(0) −0.50	0.80	0.46	0
Δ_{fuel}	WL-M	(1.66) 4.14	(0.19) 2.64	(0) 2.45	3.79	0.26	0
Δ_{fuel}	WL-H	(3.54) 4.04	(0.12) 0.61	(0) 0.48	1.85	0.16	0
Δ_{fuel}	WL-E	(1.87) 2.15	(0.17) 0.44	(0) 0.27	1.79	0.11	0

provements that approach 4% over the constant voltage control.

The DC-link dynamic voltage variation implementation in the realistic setting of a high fidelity simulation model, reveals that complex nonlinear dynamics can arise by the coupling of the various powertrain component dynamics and saturating behaviour, the supervisory control, and the optimized voltage control. Special measures in the design of the variable voltage controls are taken and alleviate effectively this coupling and undesirable nonlinear dynamics.

References

[1] Committee on Climate Change, Reducing emissions and preparing for climate change – 2015 Progress Report to Parliament 2, www.theccc.org.uk/.

[2] O. Edenhofer, et al., Climate change 2014: Mitigation of climate change, Sci. rep., IPCC (2014).

[3] B. K. Bose, Global energy scenario and impact of power electronics in 21st century, IEEE Transactions on Industrial Electronics 60 (2013) 2638–2651.

[4] A. Khaligh, A. M. Rahimi, A. Emadi, Modified pulse-adjustment technique to control dc/dc converters driving variable constant-power loads, Industrial Electronics, IEEE Transactions on 55 (3) (2008) 1133–1146.

[5] S. G. Wirasingha, A. Emadi, Classification and review of control strategies for plug-in hybrid electric vehicles, Vehicular Technology, IEEE Transactions on 60 (1) (2011) 111–122.

[6] J. O. Estima, A. J. M. Cardoso, Efficiency analysis of drive train topologies applied to electric/hybrid vehicles, IEEE Transactions on Vehicular Technology 61 (2012) 1021–1031.

[7] S. Dusmez, A. Hasanzadeh, A. Khaligh, Loss analysis of non-isolated bidirectional dc/dc converters for hybrid energy storage system in evs, in: Industrial Electronics (ISIE), 2014 IEEE 23rd International Symposium on, IEEE, 2014, pp. 543–549.

[8] F. Krismer, J. Kolar, Efficiency-optimized high-current dual active bridge converter for automotive applications, IEEE Transactions on Industrial Electronics 59 (2012) 2745–2760.

[9] S. Inoue, H. Akagi, A bidirectional DC-DC converter for an energy storage system with galvanic isolation, IEEE Transactions on Power Electronics 22 (2007) 2299–2305.

[10] H. Li, F. Z. Peng, J. Lawler, A natural ZVS medium-power bidirectional DC-DC converter with minimum number of devices, IEEE Transactions on Inductry Applications 39.

[11] A. K. Rathore, U. Prasanna, Analysis, design, and experimental results of novel snubberless bidirectional naturally clamped zcs/zvs current-fed half-bridge dc/dc converter for fuel cell vehicles, Industrial Electronics, IEEE Transactions on 60 (10) (2013) 4482–4491.

[12] H. Al-Sheikh, O. Bennouna, G. Hoblos, N. Moubayed, Modeling, design and fault analysis of bidirectional dc-dc converter for hybrid electric vehicles, in: Industrial Electronics (ISIE), 2014 IEEE 23rd International Symposium on, IEEE, 2014, pp. 1689–1695.

[13] Z. Amjadi, S. S. Williamson, Power-electronics-based solutions for plug-in hybrid electric vehicle energy storage and management systems, Industrial Electronics, IEEE Transactions on 57 (2) (2010) 608–616.

[14] B. Zhao, Q. Song, W. Liu, Y. Sun, Overview of dual-active-bridge isolated bidirectional DC-DC converter for high-frequency-link power-conversion system, IEEE Transactions on Power Electronics 29 (8) (2014) 4091–4106.

[15] W. Chen, P. Rong, Z. Lu, Snubberless bidirectional DC-DC converter with new CLLC resonant tank featuring minimized switching loss, IEEE Transactions on Industrial Electronics 57 (9) (2010) 3075–3086.

[16] G. Ma, W. Qu, G. Yu, Y. Liu, N. Liang, W. Li, A zero-voltage-switching bidirectional DC-DC converter with state analysis and soft-switching-oriented design consideration, IEEE Transactions on Industrial Electronics 56 (6) (2009) 2174–2184.

[17] S. A. Evangelou, W. Shabbir, Dynamic modeling platform for series hybrid electric vehicles, in: 8th IFAC Symposium Advances in Automotive Control - AAC 2016, IFAC, Kolmarden Wildlife Resort, Sweden, 2016.

[18] H. Bai, C. Mi, Eliminate reactive power and increase system efficiency of isolated bidirectional dual-active-bridge DC-DC converters using novel dual-phase-shift control, IEEE Transactions on Power Electronics 23 (6) (2008) 2905–2914.

[19] G. Oggier, G. O. Garca, A. R. Oliva, Modulation strategy to operate the

dual active bridge dc-dc converter under soft switching in the whole operating range, IEEE Transactions on Power Electronics 26 (4) (2011) 1228–1236.

[20] F. Krismer, S. Round, J. W. Kolar, Performance optimization of a high current dual active bridge with a wide operating voltage range, in: Power Electronics Specialists Conference. 37th IEEE, 2006, pp. 1–7.

[21] H. Zhou, A. M. Khambadkone, Hybrid modulation for dual-active-bridge bidirectional converter with extended power range for ultracapacitor application, IEEE Transactions on Industry Applications 45 (4) (2009) 1434–1442.

[22] B. Zhao, Q. Song, W. Liu, Efficiency characterization and optimization of isolated bidirectional DC-DC converter based on dual-phase-shift control for DC distribution application, IEEE Transactions on Power Electronics 28 (4) (2013) 1711–1727.

[23] H. Wen, B. Su, Reactive power and soft-switching capability analysis of dual-active-bridge DC-DC converters with dual-phase-shift control, Journal of Power Electronics 15 (1) (2015) 18–30.

[24] Y. Song, B. Wang, Evaluation methodology and control strategies for improving reliability of hev power electronic system, Vehicular Technology, IEEE Transactions on 63 (8) (2014) 3661–3676.

[25] M. Roche, W. Shabbir, S. A. Evangelou, Voltage control for enhanced power electronic efficiency in series hybrid electric vehicles, IEEE Transactions on Vehicular Technology.

[26] Y. C. Wang, Y. C. Wu, T. L. Lee, Design and implementation of a bidirectional isolated dual-active-bridge-based DC/DC converter with dual-phase-shift control for electric vehicle battery, in: 2013 IEEE Energy Conversion Congress and Exposition, 2013, pp. 5468–5475.

[27] M. Kim, M. Rosekeit, S. K. Sul, R. W. A. A. De Doncker, A dual-phase-shift control strategy for dual-active-bridge dc-dc converter in wide voltage range, in: Power Electronics and ECCE Asia, IEEE 8th International Conference on, 2011, pp. 364–371.

[28] W. Shabbir, Control strategies for series hybrid electric vehicles, Ph.D. thesis, Imperial College London (2016).

[29] S. A. Evangelou, A. Shukla, Advances in the modelling and control of series hybrid electric vehicles, in: Proceedings of 2012 American Control Conference, IEEE, Montreal, Canada, 2012.

[30] S. A. Evangelou, M. A. Rehman-Shaikh, Power loss characterization of bidirectional DC-DC converter with dual-phase-shift controlIn review.

[31] M. Ehsani, Y. Gao, A. Emadi, Modern electric, hybrid electric, and fuel cell vehicles: fundamentals, theory, and design, CRC Press, 2010.

[32] Y. Ko, J. Lee, H. Lee, A supervisory control algorithm for a series hybrid vehicle with multiple energy sources, Vehicular Technology, IEEE Transactions on 64 (11) (2015) 4942–4953.

[33] W. Shabbir, S. A. Evangelou, Real-time control strategy to maximize hybrid electric vehicle powertrain efficiency, Applied Energy 135 (2014) 512 – 522.

[34] N. Mohan, T. Undeland, W. Robbins, Power Electronics: Converters, Applications and Design, John Wiley and Sons, 2003.

[35] D. Graovac, M. Purschel, IGBT power losses calculations using datasheet parameters, Tech. rep., Infineon Technologies (2009).

[36] M. H. Bierhoff, F. W. Fuchs, Semiconductor losses in voltage source and current source IGBT converters based on analytical derivation, in: Power Electronics Specialists Conference (PESC 04), IEEE 35th Annual, Vol. 4, 2004, pp. 2836–2842. doi:10.1109/PESC.2004.1355283.

[37] M. A. Rehman-Shaikh, Investigation of FACTS devices to improve power quality in distribution networks, Ph.D. thesis, Imperial College London (2010).

[38] M. Kheraluwala, R. Gascoigne, D. Divan, E. Baumann, Performance characterization of a high power dual active bridge DC-DC converter, IEEE Transactions on Industry Applications 28 (1992) 1294–1301.

[39] Nanocrystalline soft magnetic material FINEMET, http://www.hilltech.com/pdf/hl-fm10-cFinemetIntro.pdf (2016). URL http://www.hitachi-metals.co.jp/products/elec/tel/pdf/hl-fm9-h.pdf

[40] W. A. Roshen, A practical, accurate and very general core loss model for nonsinusoidal waveforms, IEEE Transactions on Power Electronics 22 (1) (2007) 30–40.

[41] The International Council on Clean Transportation, The WLTP: How a new test procedure for cars will affect fuel consumption values in the EU (Working paper 2014-9), http://www.theicct.org/sites/default/files/publications/ICCT_WLTP_EffectEU_20141029.pdf.

[42] A. Sciarretta, M. Back, L. Guzzella, Optimal control of parallel hybrid electric vehicles, IEEE Transactions on Control Systems Technology 12 (3) (2004) 352–363.

[43] L. Serrao, S. Onori, G. Rizzoni, ECMS as a realization of pontryagin's minimum principle for HEV control, in: 2009 American Control Conference, 2009, pp. 3964–3969.